In situ synchrotron radiation μCT indentation of cortical bone: Anisotropic crack propagation, local deformation, and fracture

Marta Peña Fernández, Jakob Schwiedrzik, Alexander Bürki, Françoise Peyrin, Johann Michler, Philippe K Zysset, Uwe Wolfram

Acta Biomaterialia 167 (2023) 83–99

Contents lists available at ScienceDirect

Acta Biomaterialia

journal homepage: www.elsevier.com/locate/actbio

Full length article

In situ synchrotron radiation μCT indentation of cortical bone: Anisotropic crack propagation, local deformation, and fracture

Marta Peña Fernández[a,1], Jakob Schwiedrzik[b,1], Alexander Bürki[c], Françoise Peyrin[d], Johann Michler[b], Philippe K. Zysset[c], Uwe Wolfram[a,*]

[a] School of Engineering and Physical Science, Institute for Mechanical, Process and Energy Engineering, Heriot-Watt University, Edinburgh, United Kingdom
[b] Empa, Swiss Federal Laboratories for Materials Science and Technology, Laboratory for Mechanics of Materials and Nanostructures, Thun, Switzerland
[c] ARTORG Centre for Biomedical Engineering Research, University of Bern, Bern, Switzerland
[d] Université de Lyon, INSA Lyon, Université Claude Bernard Lyon 1, UJM-Saint Etienne, CNRS UMR 5220, Inserm U1294, CREATIS, Lyon, France

ARTICLE INFO

Article history:
Received 31 January 2023
Revised 21 April 2023
Accepted 25 April 2023
Available online 29 April 2023

Keywords:
Cortical bone
Indentation
Synchrotron X-ray radiation
micro-computed tomography
Digital volume correlation
Fracture behaviour

ABSTRACT

The development of treatment strategies for skeletal diseases relies on the understanding of bone mechanical properties in relation to its structure at different length scales. At the microscale, indention techniques can be used to evaluate the elastic, plastic, and fracture behaviour of bone tissue. Here, we combined *in situ* high-resolution SRμCT indentation testing and digital volume correlation to elucidate the anisotropic crack propagation, deformation, and fracture of ovine cortical bone under Berkovich and spherical tips. Independently of the indenter type we observed significant dependence of the crack development due to the anisotropy ahead of the tip, with lower strains and smaller crack systems developing in samples indented in the transverse material direction, where the fibrillar bone ultrastructure is largely aligned perpendicular to the indentation direction. Such alignment allows to accommodate the strain energy, inhibiting crack propagation. Higher tensile hoop strains generally correlated with regions that display significant cracking radial to the indenter, indicating a predominant Mode I fracture. This was confirmed by the three-dimensional analysis of crack opening displacements and stress intensity factors along the crack front obtained for the first time from full displacement fields in bone tissue. The X-ray beam significantly influenced the relaxation behaviour independent of the tip. Raman analyses did not show significant changes in specimen composition after irradiation compared to non-irradiated tissue, suggesting an embrittlement process that may be linked to damage of the non-fibrillar organic matrix. This study highlights the importance of three-dimensional investigation of bone deformation and fracture behaviour to explore the mechanisms of bone failure in relation to structural changes due to ageing or disease.

Statement of significance

Characterising the three-dimensional deformation and fracture behaviour of bone remains essential to decipher the interplay between structure, function, and composition with the aim to improve fracture prevention strategies. The experimental methodology presented here, combining high-resolution imaging, indentation testing and digital volume correlation, allows us to quantify the local deformation, crack propagation, and fracture modes of cortical bone tissue. Our results highlight the anisotropic behaviour of osteonal bone and the complex crack propagation patterns and fracture modes initiating by the intricate stress states beneath the indenter tip. This is of wide interest not only for the understanding of bone fracture but also to understand other architectured (bio)structures providing an effective way to quantify their toughening mechanisms in relation to their main mechanical function.

* Corresponding author: School of Engineering and Physical Sciences, Institute of Mechanical, Process and Energy Engineering, Heriot-Watt University, EH14 4AS, Edinburgh, UK.
E-mail address: u.wolfram@hw.ac.uk (U. Wolfram).
[1] These authors share first authorship

https://doi.org/10.1016/j.actbio.2023.04.038
1742-7061/

1. Introduction

Bone is a stiff, strong, and tough multifunctional material primarily composed of water, collagen, and hydroxyapatite. Its highly hierarchical structure determines its mechanical properties at different length scales [1]. At the macroscale, bone consist of a dense and hard cortical shell enclosing a trabecular core, with cortical bone playing a major role in determining the overall mechanical competence [2]. Cortical bone is composed by osteonal and interstitial bone. Osteons are cylindrical structures made of concentric lamellae that surround and protect blood vessels. Each individual lamella comprises bundles of mineralised collagen fibrils orientated at different angles to the osteon axis in a plywood-type motif [3–5]. The resistance of bone to fracture originates from the multiple deformation and toughening mechanisms that span across several length scales. However, as the risk of bone fracture increases with ageing [6–9] and disease [10], it remains essential to understand the mechanisms of bone failure in relation to these structural length scales to develop treatment strategies that prevent or reverse these negative effects.

Indentation techniques are widely used to evaluate bone mechanical properties from tissue to lamellar length scales [11]. Properties of bone such as hardness and elastic modulus can be extracted from the indentation curves [12], while the yield properties may be assessed using inverse methods [13,14]. However, the analysis of the plastic deformation during indentation is complex due to the multiaxial stress state present in the deformation zone below the indenter tip. Such stresses develop differently during indentation depending on the indenter shape and the anisotropic tissue organisation. While spherical tips minimise the plastic deformation and damage, providing a smooth transition from elastic to elasto-plastic contact, Berkovich tips induce plasticity at very small loads and the measured mechanical properties are, therefore, more sensitive to damage in comparison to indentation tests with spherical tips [15]. In that perspective, a simultaneous analysis of bone deformation under different indenter geometries may provide greater insight on the damage mechanisms, i.e., microcrack development, leading to bone fracture.

A key advantage of indentation testing relies on the robustness of the technique and the possibility to rapidly screen large areas of complex heterogeneous materials such as bone, allowing to probe localised microstructural features. As such, indentation testing has grown popularity for the evaluation of both local and bulk fracture properties of hard tissues by making direct measurements of cracks created using sharp indenter tips [16–22]. However, this technique remains semi-quantitative for fracture toughness evaluation [23]. Moreover, most indentation tests have so far restricted the examination of cracks to the material surface upon unloading using scanning electron microscopy [22,24], thus, hindering the deformation analysis of the material below the indenter tip during indentation. Recent *in situ* micro-computed tomography (μCT) indentation tests have proved to be useful to visualise the three-dimensional (3D) cracking and fracture behaviour not only in bone [25,26], but also in dentin [27], and non-biological brittle materials [28,29]. Most importantly, the deformation beneath the indenters could be measured by digital volume correlation (DVC) of the acquired tomographs [25,27,29].

The combination of high-resolution μCT and DVC remains unique for the assessment of the 3D structure-function relationships in materials undergoing deformation, and has, therefore, been previously used to study the deformation patterns of cortical bone specimens loaded in compression [30–32], during fracture toughness testing [33], and following indentation loading [25]. Karali et al. [25] recently showed that cortical bone specimens indented in the axial direction developed larger cracks and higher residual strains compared to those indented in the transverse direction using a lab-based μCT system. However, the specimens were imaged after the indenter was retracted, thus the strain distribution under indentation loading was not evaluated. Moreover, the limited spatial resolution, hindered the analysis of the deformation beneath the indenter tip, as well as the crack propagation patterns in relation to cortical bone microstructural features. To gain a better insight of the deformation mechanisms at the tissue level and the crack paths developing under the indenter tip, image resolutions in the order of one micrometre that can be achieved using synchrotron radiation (SR)μCT remains essential [32,33] as this helps to improve the DVC-spatial resolution, and consequently the displacement and strain field accuracy [34], and allow us to quantitatively analyse crack propagation in cortical bone.

The displacement field around cracks quantified using DVC provide the necessary information to measure crack opening displacements [29,32], modes of fracture, and stress intensity factors near the crack tip [35–37]. To our knowledge, only one study has assessed the crack opening displacements in cortical bone [32]. Christen et al. [32] evaluated crack opening displacements up to 2 μm in murine pre-notched femurs loaded in compression. Yet, the analysis was restricted to 20 SRμCT cross-sections, and stress intensity factors and local modes of fracture have not been observed. This information is important to measure local toughening mechanisms at the crack tip and to improve our current understanding of crack growth in relation to cortical bone microstructure.

Here, we aim to investigate (1) the influence of the indenter tip shape and tissue orientation on the cracking behaviour and local deformation of cortical bone under indentation loading, and (2) the local fracture properties obtained from experimental displacement fields around indentation-induced cracks. To do so (1) we combine stepwise *in situ* SRμCT indentation testing and DVC to explore the interplay between crack initiation and local deformation under spherical and Berkovich indenters in ovine cortical bone; (2) we quantify local crack opening displacements, fracture modes, and stress intensity factors at indentation-induced crack tips from the DVC-measured displacements fields. This will ultimately serve to evaluate the elastic, plastic, and fracture behaviour of bone in relation to its microstructure. We anticipate that this experimental technique will improve our understanding of indentation tests and their results and will be applicable to a wide variety of hard tissues.

2. Materials and methods

2.1. Specimens

60 cylindrical specimens were produced from ovine cortical bone. Parallelepipeds of approximately 4 × 4 × 35 mm were cut from the femoral diaphysis of mature animals along (axial) and transverse to the diaphyseal main direction using a high precision band saw (EXACT, Germany). The parallelepipeds were dried at ambient temperature for 24 h and then trimmed into approximately 4 mm long sections which were glued on aluminium cylinders with 8 mm diameter and 12 mm height using cyanoacrylate. To reduce weight the aluminium cylinders featured a blind hole of 5 mm diameter and 10 mm depth. Parallelepipeds were then lathed to 3 mm diameter cylinders using a desktop lathe (PROMAC, Taiwan). These cylinders were subsequently milled to approximately 4 mm height with an ultra-miller (Leica, Germany) so that the surfaces at the free ends were flat and smooth.

2.2. Stepwise indentation and SRμCT imaging

A custom-made indentation device was used in this study Figure S1. The dry samples were loaded in stepwise manner in three

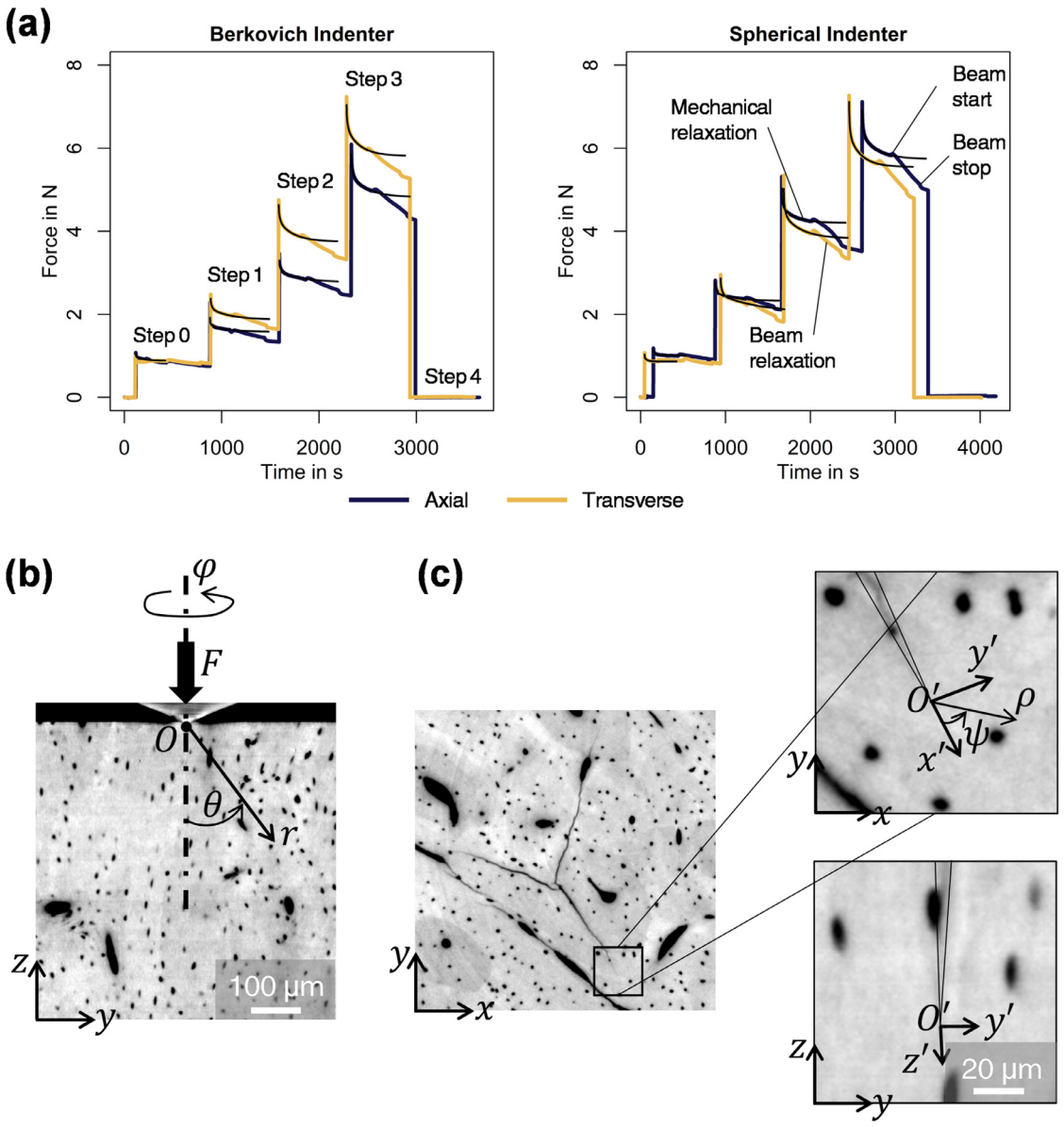

Fig. 1. (a) Exemplary force-time curves of four different specimens illustrating the stepwise loading for the two different indenters and the two different load directions. The thin black curves extrapolate the mechanical relaxation period to illustrate the expected relaxation behaviour without the beam. For this, non-normalised Prony-series $F = F_\infty + \sum_{i=1}^{3} F_i exp(^{-t}/_{\tau_i})$ with F_∞ long-term force, F_i force parameters, and τ_i characteristic time were fitted to the 5 min relaxation data. (b, c) Schematic of local coordinate system (b) around the indenter tip and (c) crack tip in an exemplary bone specimen indented with a Berkovich tip in the axial direction. The SRµCT cross-sections shows the vascular porosity (black), the primary osteons (dark grey), the interstitial tissue (light grey), and the cellular porosity (i.e., osteocyte lacunae) visible as small black ellipsoids. Crack systems under the indenter tip are also seen in (c). (For interpretation of the references to colour in this figure legend, the reader is referred to the web version of this article.)

load steps with approximately 10 µm displacement per load step (Fig. 1a). After each load step a waiting time of 5 min was introduced to minimize sample creep induced drift in the imaging data. Cylinders with either axial or transverse material orientation were tested with two different custom made indenter tips. A Berkovich tip with an indentable height of 30 µm and a sphero-conical diamond tip with a cone angle of 90° and a cone radius of 100 µm (Synthon MDP, Switzerland) were used. Prior to loading, a SRµCT scan was acquired to image the unloaded configuration. Subsequently, the sample was imaged after each load step. A final scan was acquired following unloading of the sample. This resulted in five scans in total per tested sample.

We performed SR phase-contrast µCT on beamline ID19 at European Synchrotron Radiation Facility (ESRF) using a harmonic 31 keV and 200 mA (7/8 multibunch mode) setup with 1499 projections over 360° angular range and a shutter time of 0.2 s. No monochromators were used. Instead, the peak was isolated from the undulator source U17.6 with a specific filter combination (2 mm Aluminium + 0.25 mm Cu + gap 15 mm). Source to detector distance was 145,000 mm and sample to detector distance was 40 mm. The transmitted X-ray beam was captured with a 2048 × 1024 CCD FReLoN detector [38] that was mounted behind a Europium doped Gadolinium Gallium Garnet scintillator with a thickness of 10 µm and a microscope optics with a 10 × objective (NA 0.3) and a 2 × eyepiece. To facilitate fast read out, we operated the camera in frame-transfer mode (see [39] for more details).

Phase retrieval was performed using Paganin's algorithm [40] with a δ/β of 3/1. 3D reconstructions were performed us-

ing pyHST (python High Speed Tomography), an ESRF specific implementation of a filtered back projection [41]. Ring artefacts were corrected using a custom-made MATLAB (MathWorks, Massachusetts) software [42] in two steps (Table S1). Reconstruction was performed using 4 GPU Tesla C1060 cards with 240 processors per GPU. Datasets of 2048×2048×1024 were reconstructed in approximately 240 s. The resulting isotropic voxel size in the images was 670 nm.

2.3. Image analysis

We performed all image processing operations to segment bone tissue, vascular and cellular porosity, microcracks, indenter, and air using ITK, Python, NumPy, scikit-image and SimpleITK [43–45]. Details on image segmentation may be found in the supplementary material Section

2.3.1. Contact depth, contact area, and hardness

To determine the contact depth, we combined the masks of air and indenter and applied a closing operation. We fitted a plane to the surface voxels and its distance to the known indenter position was taken as the indentation depth, h. We determined the area at maximum indentation depth by the equations $A = \pi(2Rh - h^2)$ for the sphero-conical indenter and $A = 24.5h^2$ for the Berkovich indenter [46]. We calculated hardness as the force at the end of the relaxation time divided by the area at maximum indentation depth at each loading step.

2.3.2. Microcrack systems

To compare microcrack systems under the indenter tips, we determine slice-wise polar plots for each tested specimen and for load steps 1, 2, and 3 at 360 angular steps. For each angular step, the microcrack voxels lying on a Bresenham line were counted. The length of the line corresponded to the radius of the largest possible circle around the indenter apex. We projected the slice-wise polar plots on one plane and load steps 1,2, and 3 were overlaid to illustrate microcrack propagation.

2.3.3. Cellular porosity

We analysed the cellular volume in a 300×300×300 voxel (201×201×201 μm^3) volume of interest (VOI) centred under the indenter tip. The VOI started at the specimen surface so that sink-in during the indentation was compensated. The cell porosity, Φ, was determined from the segmented images following Eq. (1), where V_{cells}, V_{tip} and V_{air} represent the volume occupied by the cells, the indenter tip, and the air, respectively, within the defined VOI. We used linear regressions to identify possible correlations between pore closure and indentation depth.

$$\Phi = \frac{V_{cells}}{VOI - V_{tip} - V_{air}} \tag{1}$$

2.4. Digital volume correlation

We performed DVC analysis (DaVis v8.4, LaVision, Germany) on the SRμCT images after masking out the indenter tip and air to investigate the displacement and strain fields underneath the indenter tip at increasing indentation depth. We used the image acquired at step 0 as a reference. The DaVis software is based on a local approach of deformable registration, and details on the operating principles of the algorithm have been extensively reported elsewhere [47,48]. The image volumes were correlated using a multipass scheme that used the displacement gradient from the previous pass to deform the subvolumes on the subsequent passes. A Fourier-fast-transform pre-shift window of 112 voxels size preceded a direct correlation DVC computation with decreasing subvolume sizes (i.e., interrogation window) of 64, 56, 48 and 40 voxels with 75%, 50%, 50% and 0% overlap between subvolumes, respectively, and two passes for each step was used. These parameters were found to be optimal (Supplementary Material, section S4) with correlation coefficient > 0.9, random errors in the displacements not exceeding 0.082 μm, and accuracy and precision of the strain components [48–50] of 2.3 × 10^{-4} and 7.7 × 10^{-5}, respectively.

Rigid body motion due finite frame compliance was removed by geometrical transformation of the DVC-obtained displacement field, setting the relative displacement between load steps 0 and 1 to zero at their base, where the deformation due to indentation should be negligible. From the resulting displacement fields, the strain tensor was derived and expressed in spherical coordinates (radial, ε_r, hoop, ε_φ, and circumferential ε_θ, directions), with the origin of the reference system located at the indenter tip, $O = (x_t, y_t, z_t)$ (Fig. 1b).

2.5. Crack opening displacements and stress intensity factors

We investigated the crack opening displacements and stress intensity factors in five samples indented with the Berkovich tip in axial direction. This selection was based on cracks that propagated radially from the indenter edges (i.e., peaks were visible at given angles in the polar plots) and that did not extend outside the analysed field of view. Moreover, we excluded short cracks (< 50 μm) that mostly remained within the plastic deformation zone of the indent. In total, we analysed the front of 14 cracks (two at load step 2 and 12 at load step 3).

For each of the cracks analysed, the displacement field in the original coordinate system (u_x, u_y, u_z) was transformed to a local coordinate system centred at the crack tip $(u_{x'}, u_{y'}, u_{z'}) = (u, v, w)$ (Fig. 1c). The crack opening displacements were estimated from the DVC-computed displacement difference between two planes taken parallel on either side of the crack [37]. To avoid image correlation errors due to the discontinuity, the two planes were chosen at a distance of 100 voxels (67 μm), which were sufficiently remote from the crack [29].

We extracted the stress intensity factors from the elastic K-dominated field of the cracks of interest following previous approaches [35–37]. First, we assumed that each plane orthogonal to the indentation loading axis (nearly orthogonal to the mean direction of the crack front, (x, y) plane in Fig. 1c), could be treated separately [36,37]. For each of these planes, the crack-tip displacement fields can be expressed as a Williams [51] expansion of the following form:

$$\begin{pmatrix} u_I \\ v_I \end{pmatrix} = \begin{pmatrix} \sum_{n=1}^{\infty} \frac{a_n}{2\mu\sqrt{2\pi}} \rho^{\frac{n}{2}} \left[\left(\kappa + \frac{n}{2} + (-1)^n\right) \cos\frac{n\psi}{2} - \frac{n}{2}\cos\frac{(n-4)\psi}{2} \right] \\ \sum_{n=1}^{\infty} \frac{a_n}{2\mu\sqrt{2\pi}} \rho^{\frac{n}{2}} \left[\left(\kappa - \frac{n}{2} - (-1)^n\right) \sin\frac{n\psi}{2} + \frac{n}{2}\sin\frac{(n-4)\psi}{2} \right] \end{pmatrix} \tag{2}$$

for Mode I, and

$$\begin{pmatrix} u_{II} \\ v_{II} \end{pmatrix} = \begin{pmatrix} -\sum_{n=1}^{\infty} \frac{b_n}{2\mu\sqrt{2\pi}} \rho^{\frac{n}{2}} \left[\left(\kappa + \frac{n}{2} - (-1)^n\right) \sin\frac{n\psi}{2} - \frac{n}{2}\sin\frac{(n-4)\psi}{2} \right] \\ \sum_{n=1}^{\infty} \frac{b_n}{2\mu\sqrt{2\pi}} \rho^{\frac{n}{2}} \left[\left(\kappa - \frac{n}{2} + (-1)^n\right) \cos\frac{n\psi}{2} + \frac{n}{2}\cos\frac{(n-4)\psi}{2} \right] \end{pmatrix} \tag{3}$$

for Mode II, where (u, v) are the displacements in the crack coordinate system (Fig. 2b), μ is the second Lamé's coefficient ($\mu = E/2(1-\upsilon)$), κ is the Kolossov's constant ($\kappa = (3-\upsilon)/(1-\upsilon)$ for

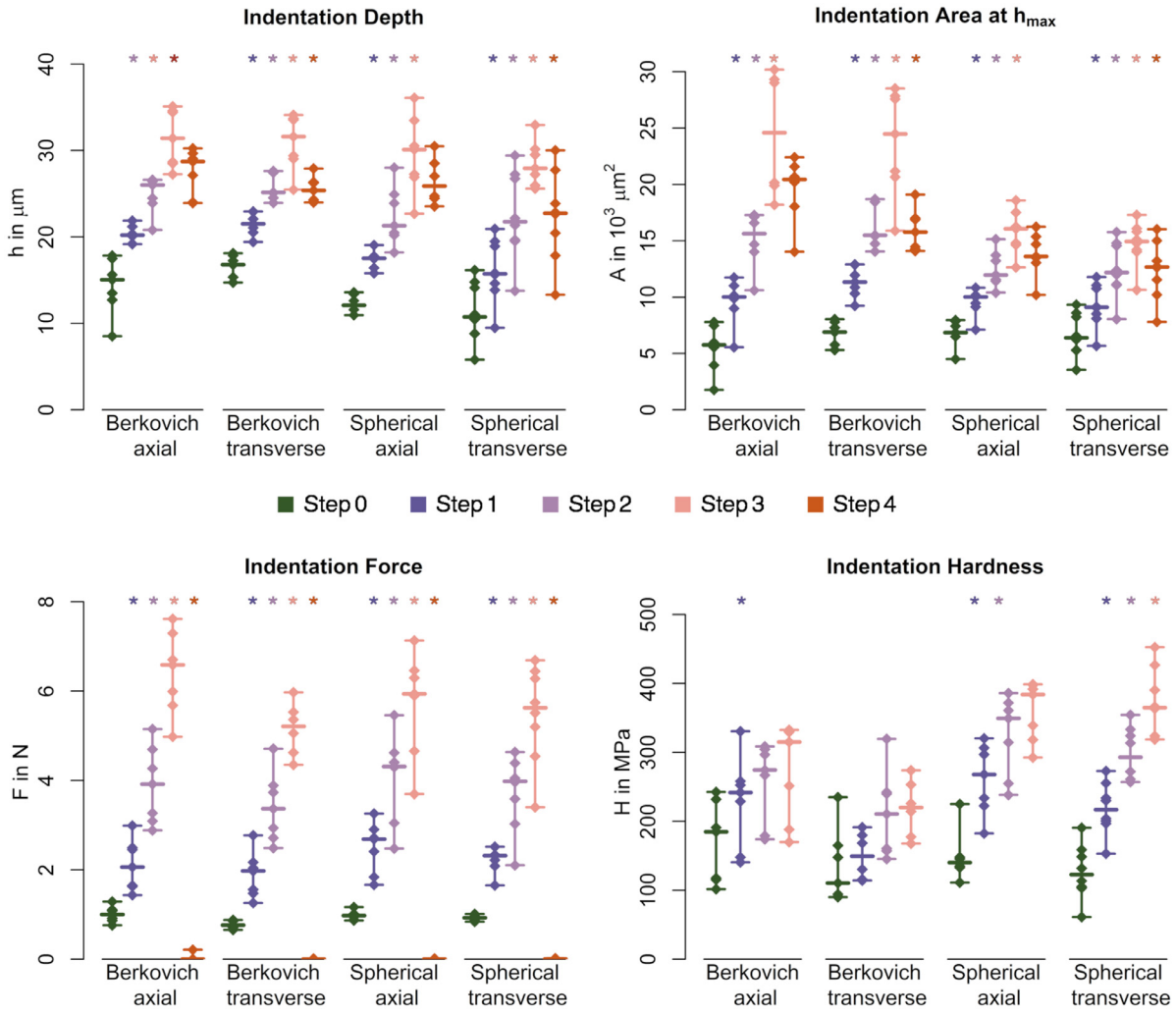

Fig. 2. Descriptive indentation data for all load steps 0 to 4. Load step 0 was defined as unloaded situation. However, an initial deformation is present due to the loading protocol where contact was defined to be established as soon as a small load (≤1 N) was detectable. Load step 4 was the unloading step to zero force. * indicates significant differences to the previous load step.

plane stress conditions, and $\kappa = 3 - 4\upsilon$ for plane strain conditions), ρ and ψ are the coordinates of a point in the local cylindrical system with origin at the crack tip, O', (Fig. 1c) and E and υ are the elastic modulus and Poisson's ratio of bone. Here we assumed $E = 20\ GPa$ [52–54] and $\upsilon = 0.3$ [15].

The factor $\sqrt{2\pi}$ is introduced to match the standard singular crack field definition [55] obtained for $n = 1$, so that the amplitudes a_1 and $b_1$correspond to the stress intensity factors in Mode I, K_I, and Mode II, K_{II}, respectively.

Out of plane motions, w, induced by Mode III displacement can be defined as [37]:

$$w_{III} = \frac{K_{III}}{2\mu\sqrt{2\pi}}\ \rho^{\frac{1}{2}} sin\frac{\psi}{2} \tag{4}$$

with K_{III} the stress intensity factor in Mode III.

We used a least-square regression to fit the crack opening displacement data on either side of the crack ($\psi = \pm 180^{\circ}$) in a region extending 250 µm underneath the indenter tip to Eqs. (2)-(4) to extract K_I, K_{II}, and K_{III}. Elastic fields up to the order $n = 5$ were considered. We excluded fits with $r^2 < 0.8$. We assumed plane strain conditions, given that our sample diameters (3 mm) were $> 2.5(K/\sigma_y)^2$, which is ~ 0.25 mm (for an average crack initiation toughness of 1 MPam$^{0.5}$ and a yield stress, σ_y, of 100 MPa [33]. Additionally, we excluded planes where the in-plane measured crack length was shorter than 50 µm to ensure that the crack extension was greater than the plastic zone size around the crack tip, $r_y = \frac{1}{2\pi}(K/\sigma_y)^2$in plane strain conditions [56], which is ~10 µm.

2.6. Irradiation-induced damage

We evaluated the force-time signal during beam exposure. Visual inspection of the force-time data suggested a linear decay of the force signal after beam start (Fig. 1a). Therefore, a moving regression with a window width of 300 s was used and the slope with a maximum Pearson's correlation coefficient was recorded as beam relaxation rate, K, in N/s.

We performed Raman spectroscopy on six irradiated samples post-test and six untested specimens not exposed to SRµCT to investigate a possible influence of the beam on sample composition. Raman spectra were collected using a commercial confocal system (Nova Spectra, NT-MDT, Russia), equipped with a 100X objective (Olympus, NA 0.95) and 632 nm HeNe laser excitation source. We made ten separate measurements on each irradiated and non-irradiated sample using a 60 s integration time (single acquisition) and a 600/600 grating with approximately 2.7 cm^{-1} spectral resolution. In addition, we obtained detailed spectra around the amide I and III peaks using a 1200s integration time (single acquisition) and a finer 1800/500 grating with approximately 0.3 cm^{-1} spec-

tral resolution. The laser power at the sample surface was approximately 0.7 mW. To account for autofluorescence, the Raman spectra were baseline corrected following James et al. [57] using SpecTools.

We analysed the v_1PO_4, v_2PO_4, amid I, and amid III bands with respect to full width half maximum (FWHM), peak intensity, integrated peak area, and peak position following Mirzaali et al. [9]. We averaged and treated the data in a repeated measures analysis to reduce the variance in a sample with a limited number of specimens [58].

2.7. Statistical analysis

Indentation and imaging data were grouped in Berkovich axial, Berkovich transverse, spherical axial, and spherical transverse. Median, minimum, and maximum values for all samples within each group were computed to allow a boxplot-like representation, Data evaluation was performed with Gnu R (R Development Core Team, 2008) or python. Non-parametric tests to a significance level of $p = 0.05$ were chosen due to the small sample number.

3. Results

3.1. In situ *stepwise microindentation*

A total of 41 specimens survived mounting and could be scanned in the available beamtime. From those specimens, one specimen was lost due to beam-down in the middle of the scan, while 12 specimens were lost during the initial indentation loading, which resulted in a large initial indentation imprint. Therefore, 28 specimens, seven in four groups, were left for the analyses.

The load where we considered contact as being established induced indentations of 10 to 20 µm depth. Afterwards, indentation depth increased significantly due to external loading (Fig. 2). Median indentation depths at maximum load (i.e., load step 3) were 31.4 µm, 31.6 µm, 30.1 µm, and 27.9 µm for Berkovich axial, Berkovich transverse, spherical axial, and spherical transverse groups, respectively. Increasing indentation depth was accompanied by a significant increase in force, and indentation area. Hardness increased significantly only for the spherical indentations due to the self-similar shape of the Berkovich indenter.

3.2. Cellular porosity and crack propagation

Median cellular porosity under the tip was 4.6%, 4.4%, 4.5%, and 4.2% at the beginning and 3.5%, 3.8%, 3.7%, and 4.0% at the end of the experiment for Berkovich axial, Berkovich transverse, spherical axial, and spherical transverse, respectively (Figure S3). The cellular porosity decreased significantly for the Berkovich indenter in axial and transverse direction and for the spherical indenter in axial direction but not in transverse direction. The slope of the significant regression lines of cellular density versus indentation depth was steepest for the axial Berkovich indentations and lowest for the spherical indentations in transverse direction (Figure S4). The decrease in cellular porosity was associated with the closure of the cellular lacunae as well as an increase in crack volume underneath the indenter.

Significantly more microcracks were induced when indenting in axial than in transverse direction (Fig. 3, Figure S3). Comparing both indenter types shows that the Berkovich indentation resulted in more cracks than the spherical indentation in axial direction, but less cracks in the transverse direction (Fig. 3). The crack systems induced by the Berkovich indenter emanated from the three corners of the tip for specimens loaded in the axial direction (Fig. 4), with microcracks clearly detectable from load step 2. In the transverse direction, only small microcracks were observed, which seem to initiate from vascular canals and to propagate perpendicular to the Berkovich tip edges (Fig. 4, Figure S5). Large monodirectional crack systems were observed in the case of the spherical indenter, both in the axial and transverse direction at load step 3 (Fig. 3, Fig. 4, Figure S5). Additionally, specimens loaded in the transverse direction presented ring (cone) cracking at load step 3 (blue arrows, Fig. 4, Figure S5). Some microcracks were present before indentation, which widened with increased loading (white arrows, Figure S5).

Crack trajectories were more deflected when propagating through the transverse orientation of the specimens, while relatively linear in the longitudinal direction, independently on the indenter tip. Cracks deflected when hitting vascular canals and/or cellular lacunae (green arrows, Fig. 4, Figure S5). While most cracks penetrated the osteons, some appeared to deflect when reaching osteons (yellow arrows, Fig. 4, Figure S5). Formation of uncracked ligaments was also observed along the crack paths (orange arrows, Fig. 4, Figure S5).

3.3. Strain field mapping

DVC-computed strains showed a general increase in strain magnitude with increasing indentation load, irrespective of the indenter type and indentation direction both in the radial (Fig. 5) and hoop (Fig. 6) direction. Radial strains were axially symmetric (Video 1), reflecting the indenter profile. A region of tensile

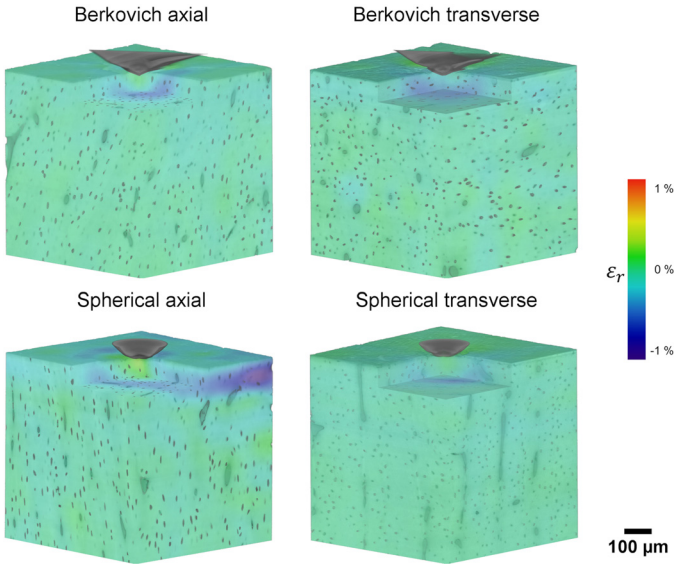

Video 1. 3D animation of radial strain,ε_r, distribution computed using digital volume correlation during indentation loading for an exemplary sample of each group (i.e., Berkovich axial, Berkovich transverse, spherical axial, and spherical transverse). The full analysed volume of interest is first shown, followed by a high-magnification of the region underneath the indenter tip.

radial strains was observed underneath both Berkovich and spherical indenter tips, which extended to ~100 µm at load step 3, and extensive compressive deformation further from the tip (Fig. 5). The built-up of radial strains was more extensive for specimens indented in the axial direction, surpassing 1% at load step 3, while those specimens indented with the Berkovich tip displayed the lowest deformation, with radial strains below 0.8% at load step 3 (Fig. 5). Hoop strains reflected the anisotropy of bone, with strains more significant for axially orientated specimens compared to transverse ones (Fig. 6, Video 2). Slice-wise polar plots demonstrated that microcracks ahead of the tip were mostly accommo-

dated by the hoop strains, with high tensile strain regions, above 2% in axially indented specimens and above 1% in transversely orientated ones, associated with Mode I cracks (Fig. 6). However, large microcracks in transverse-orientated specimens were observed in regions of large tensile radial strains, indicating a mix-mode fracture (Video 3).

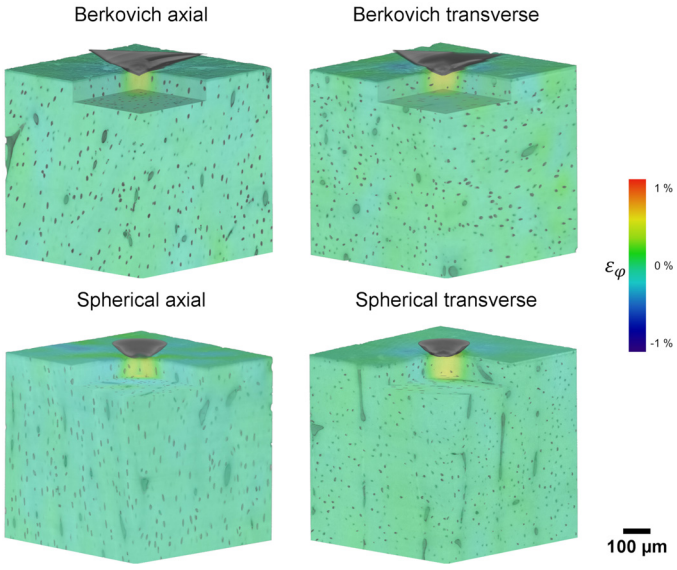

Video 2. 3D animation of hoop strain, ε_φ, distribution computed using digital volume correlation during indentation loading for an exemplary sample of each group (i.e., Berkovich axial, Berkovich transverse, spherical axial, and spherical transverse). The full analysed volume of interest is first shown, followed by a high-magnification of the region underneath the indenter tip.

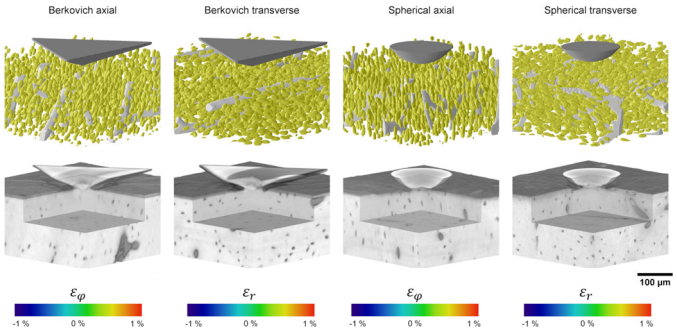

Video 3. 3D animation of the interplay between crack propagation, cortical bone microstructure and deformation for an exemplary sample of each group (i.e., Berkovich axial, Berkovich transverse, spherical axial, and spherical transverse). The top row reveals the vascular porosity (i.e., Harversian and Volkmann's canals, white), cellular porosity (i.e., cellular lacunae, yellow), and microcracks (red) developing during indentation loading underneath the indenter tip, while the bottom row shows the hoop strains, ε_φ, for axially indented samples and radial strains, ε_r, for transversely indented samples.

3.4. Crack opening displacement and stress intensity factors

The crack opening displacement data obtained from the displacement fields on either side of the cracks indicate a predominant Mode I opening (Figure S6). Median opening at the crack mouth amounted up to 1.93 µm while only up to 0.54 µm at the crack tip. Some shear displacement (Mode II) was also present, although it remained below 1.49 µm at the crack mouth and 0.68 µm at the crack tip. Out of plane motion (Mode III) was less than 0.50 µm at the crack mouth and 0.09 µm at the crack tip.

Fig. 7 shows the analysis CODs and crack driving forces in a sample indented with the Berkovich tip in the axial direction, where the front of two radial cracks was analysed at load steps 2 and 3. Crack opening displacements decreased with increasing radial and axial distance from the indenter tip (Fig. 7g, h), with an opening of ~2 µm at the crack tip 100 µm below the indenter tip (Fig. 7i). At load step 3, further propagation and consequent opening of the crack could be observed. Mode I opening was significant higher than Mode II, while out of plane motion remained close to 0 (Fig. 7i). At load step 2, K_I along the crack profile was constant, with median values of 1.1 – 1.3 MPam$^{0.5}$. Increasing the indentation load resulted in an increase of K_I, reaching values above 3 MPam$^{0.5}$ (Fig. 7h). For the blue-coloured crack in Figs. 7d-f, the larger values of K_I measured in the region extending from 50 to 100 µm below the indenter tip were consistent with the longer cracks observed. On the other hand, the large scatter of the data for the yellow-coloured cracks 50 to 150 µm below the indenter tip at both load steps 2 and 3 were associated to pre-existing microdamage in the sample (red arrow) in proximity to the crack tip.

Mode I stress intensity factors (K_I) were larger than Mode II (K_{II}) and III (K_{III}) in all analysed crack profiles (Figure S6). No correlations were observed between the measured crack length and stress intensity factors, although K_I tended to be higher for larger cracks (Figure S6). Median K_I ranged between 0.28 MPam$^{0.5}$ and 2.96 MPam$^{0.5}$, whilst median K_{II} ranged between 0.01 MPam$^{0.5}$ and 0.50 MPam$^{0.5}$, and median K_{III} between K_{III} 0.02 MPam$^{0.5}$ and 0.37 MPam$^{0.5}$.

3.5. Irradiation-induced damage

Beam relaxation rate decreased in all load steps (Figure S7). Beam relaxation was not different when comparing Berkovich and spherical indenters. Normalising beam relaxation rate to the indentation force of the respective load step showed increasing slopes for later load steps (Figure S7). Raman measurements using a relatively short integration time (60 s) was first utilised, while collecting a statistically relevant number of 10 spectra per sample. FWHM was affected by irradiation in case of all four observed variables (Figure S8). Peak height was significantly affected by irradiation in case of all observed peaks except v_1PO_4. For the integrated area under the curve differences were found for both amide peaks. Peak position changed significantly only for the amide I band. It was noted that the experimental scatter of these measures increased significantly for the irradiated samples, casting doubt on the validity of the found statistical differences. In order to verify whether or not these differences were an artefact of the strong background and the resulting decreased signal to noise ratio, further measurements using a finer spectral resolution and longer integration time (1200s) were performed for the amide I and amide III peaks on two irradiated samples and two samples in their original state. The resulting representative spectra did not yield clear differences between irradiated and non-irradiated samples (Figure S9).

4. Discussion

We combined *in situ* indentation testing with time-lapsed SRµCT and DVC to investigate microcrack systems and local deformation under a Berkovich and a spherical indenter. We performed stepwise *in situ* indentations in axial and transverse material direction, with high resolution SRµCT images acquired at increasing indentation depths. From the SRµCT data, we investigated changes in porosity due to the indentations as well as the microcrack systems emerging under the indenter due to the induced loading, while we quantified local strain fields, crack opening displacements and stress intensity factors by means of DVC of the acquired tomographs.

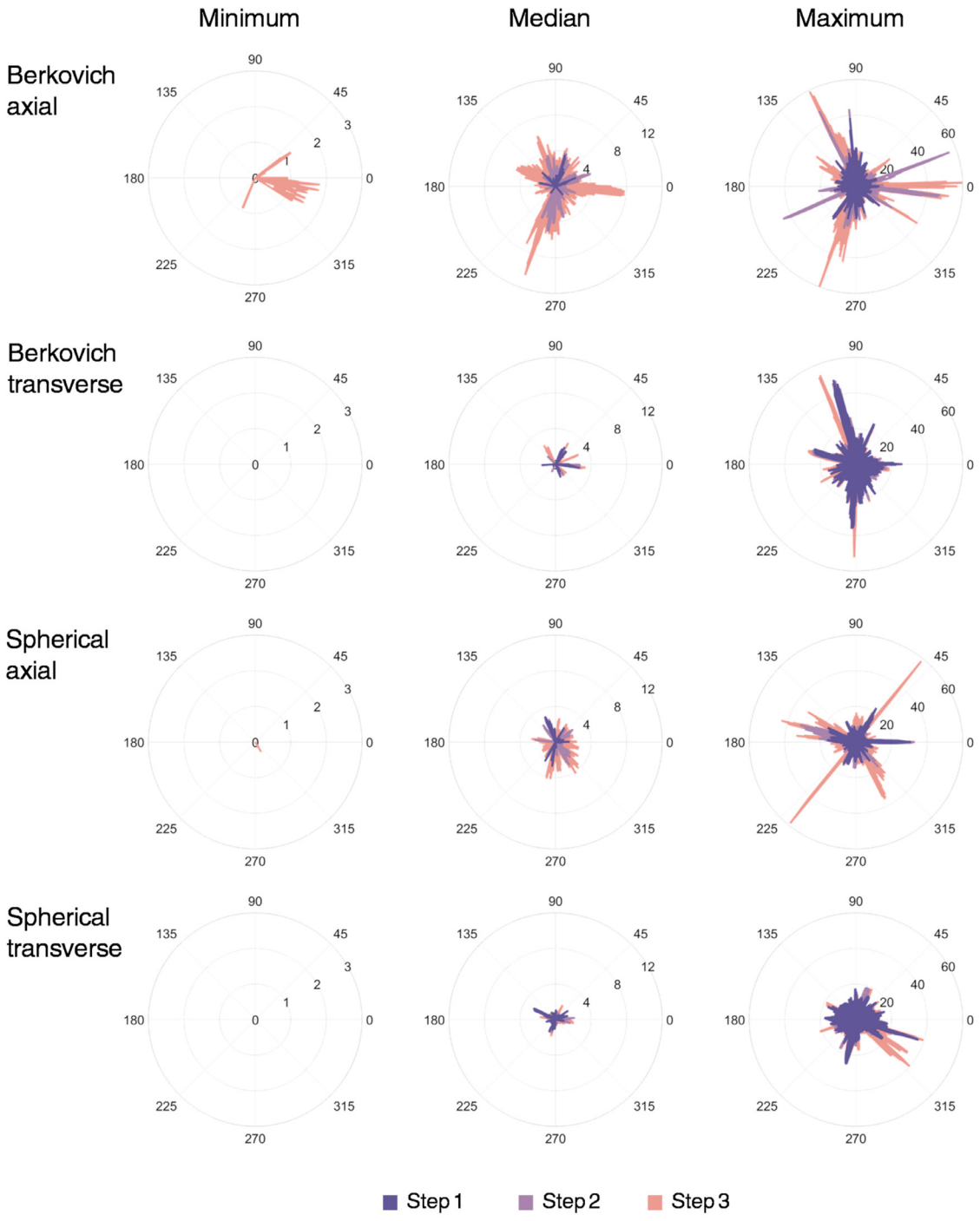

Fig. 3. Slice-wise polar plots illustrate the microcrack evolution under two different indenter tips for the two different testing directions. Crack volume in μm^3 is shown on the radial axis and angle in degrees on the angular axis.

4.1. In situ *stepwise SRμCT indentation*

The observed trends in the indentation process, such as, increasing depth and force are consistent with what could be expected for such a stepwise process. The increase in indentation area for both indenters as well as the smaller indentation area for spherical indenters are also consistent with literature on nanoindentation [15,46]. The observed trends in hardness comply with data by Schwiedrzik and Zysset [15] who reported depth-independent hardness for Berkovich indenters and increasing hardness with increasing indentation depth for spherical indenters due to their lack of self-similarity. However, loading the sample into the custom-made indenter led to considerable initial imprints on the indentation surface. A large number of samples were lost largely due to operator error when mounting the samples too fast. This resulted in several visible imprints on the indentation surface so that no clear start of the indentation process could be defined. Such samples were not further analysed.

Pore closure in the process zone (Fig. 4) may indicate densification at the cellular level. However, the used indenters lead to a stress concentration underneath the tip so that ongoing stress relaxation could blur the image due to internal flow processes. Since cellular lacunae feature a less pronounced contrast than

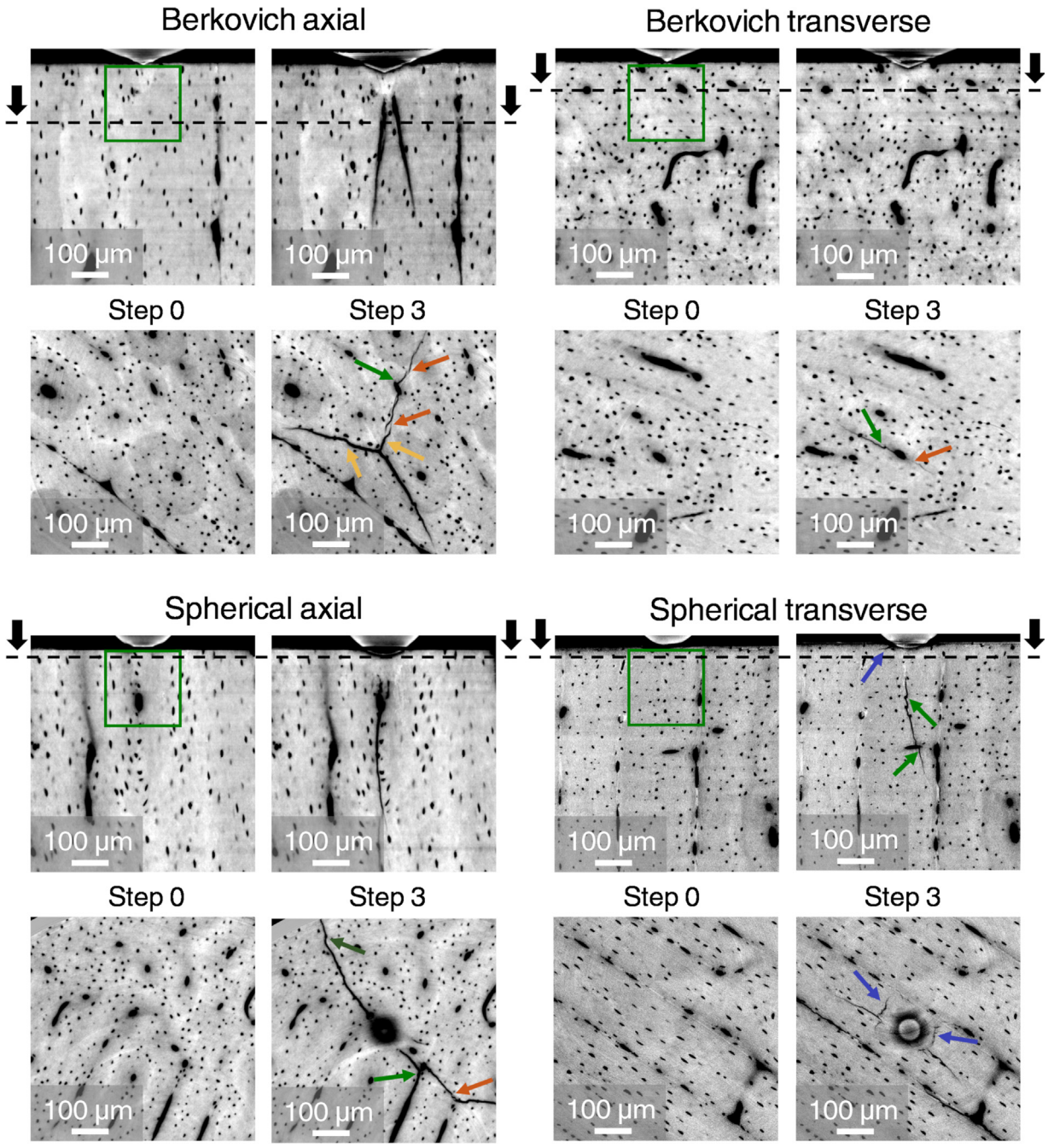

Fig. 4. Anisotropic crack propagation under Berkovich and spherical indenters. Two orthogonal SRµCT cross-sections are shown at load step 0 and load step 3, which correspond to the unloaded and maximum loading configurations, respectively. The green boxes locate the volume of interest that was used for the cellular porosity analysis. Green arrows indicate microcracks deflected as they hit vascular canals or cellular lacunae. Orange arrows point to uncracked-ligament bridging. Blue arrows indicate ring (cone) cracking under the spherical indenter. Yellow arrow points to microcrack that hit an osteon and deflected. (For interpretation of the references to colour in this figure legend, the reader is referred to the web version of this article.)

background or vascular porosity, this stress induced blurring could shadow cellular lacunae. However, the mechanical relaxation (see Prony series in Fig. 1a) seemed to be quite stable at the end of the holding time so that global relaxation may not unfold such an impact. Other studies [31,59–61], did not report diminished image quality due to such a relaxation effect when analysing trabecular and cortical bone at a coarser or similar spatial resolution. The used indenters and the achieved indentation depths are large enough to affect the analysed process zones and pores contained therein which suggests that densification is indeed taking place. In addition, pores not closed as well as emerging microcracks within the analysed zone and close to the indenter (Figs. 4, Figure S5) remain sharp and unaffected by motion artefacts. This indicates that a steady state could be assumed, and densification driven by closure of cellular pores takes place.

4.2. Anisotropic crack propagation and deformation

The observed crack maps (Figs. 4, Video 3) due to the Berkovich indenter in axial direction resemble the three-armed feature expected for the three-sided pyramid [46]. However, even indentations to similar depths (Fig. 3) lead to smaller crack systems in transverse direction (Fig. 3). Karali et al. [25] reported similar behaviour in bovine cortical bone specimens subjected to large in-

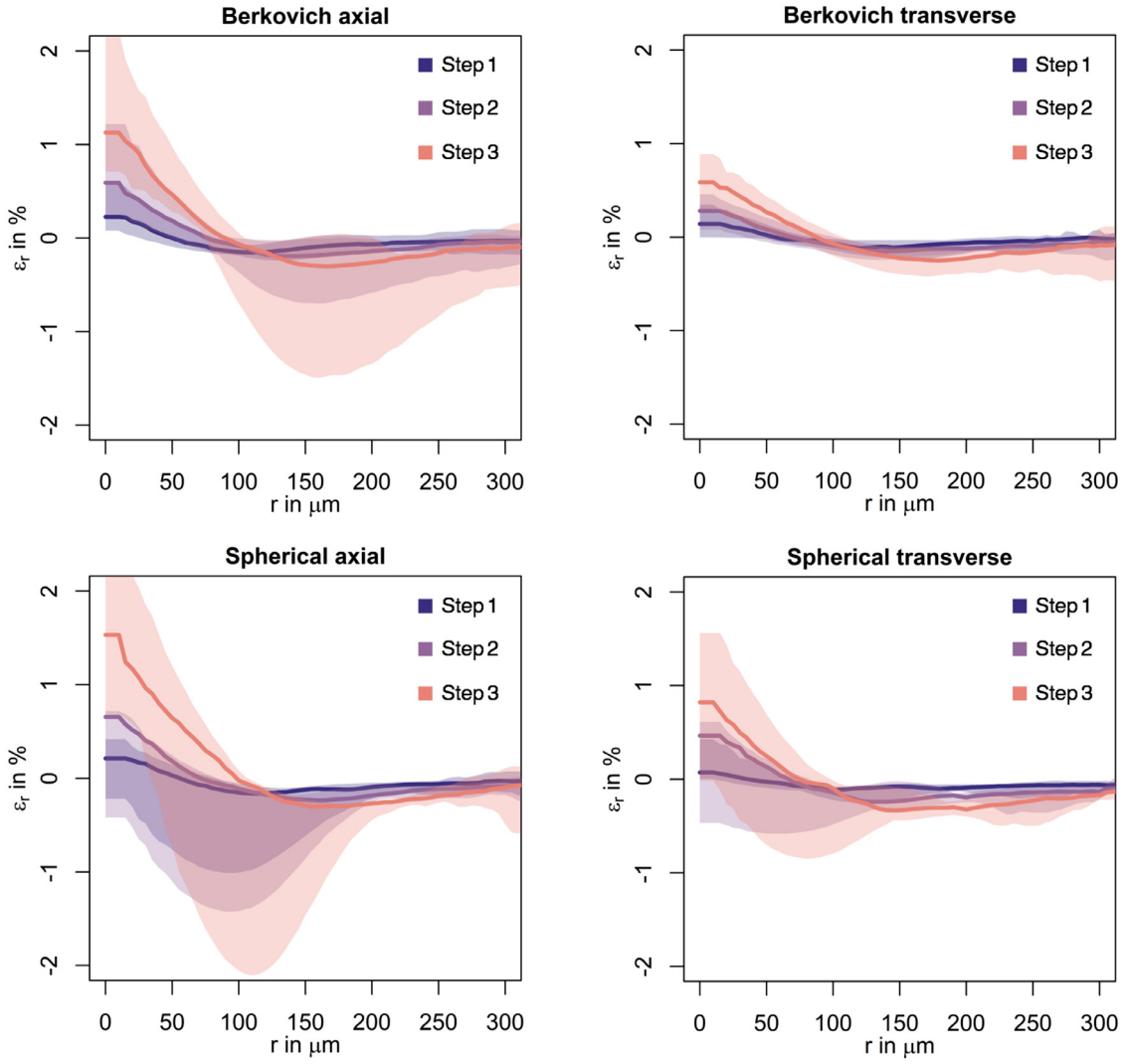

Fig. 5. Radial strains, ε_r, computed using digital volume correlation at load steps 1 to 3 as a function of the radial distance to the indenter tip. Strains were integrated over all orientations. Solid lines indicate the median strain values between specimens in each group and shaded areas the maximum and minimum strain values.

dentations in both axial and transverse direction. While the authors argued that the transverse orientation of the Harversian canals assisted in maintaining the structural integrity, the mechanism behind the differences observed in crack formation is mostly due to the underlying anisotropy of the lamellar structure [62,63] and its microstructural arrangement which features several toughening mechanisms that impede microcrack development [64]. Indeed, the fibrillar ultrastructure of ovine bone, which is largely orientated perpendicular to the indented direction in transversely orientated specimens, helps to accommodate the strain energy while providing intrinsic crack-tip shielding in the hoop direction (Video 2), inhibiting the propagation of the crack. This was previously observed in elephant dentin, where the orientation of the collagen fibrils relative to the indentation direction led to a highly anisotropic crack propagation behaviour [27]. While the difference between axial and transverse spherical indentations may follow similar arguments as in case of the Berkovich groups, the overall smaller crack systems for this indenter could be a result of indenter shape. Unlike the Berkovich pyramid, sphero-conical indenters do not feature edges that promote crack formation [46]. It is, nevertheless striking that large cracks are observable in the last loading step of the spherical indentations. These planar cracks seem to be feature-guided as they contain multiple cellular lacunae and are situated at macro-lamellar interfaces, especially in the axial case (Fig. 4). They appear as large spikes in Fig. 3 and seem to emerge at the end of the loading protocol between load step 2 and 3. This could be caused by the plastic zone underneath the indenter tip that induce tensile hoop stresses which nucleate one major crack once the material is sufficiently damaged.

We segmented microcracks in the bulk sample and applied our feature vector to decide upon a crack on each connected item in the segmentation map [65]. This robustly segments larger cracks but may lead to oversampling in case of small microcracks where, e.g., penny-shaped lacunae are segmented as well. As cracks may be guided by cellular lacunae (Fig. 4) [32,60,66] so that a lacunae connected to a crack will be sampled as part of the crack. To overcome this, a localised version of the segmentation, more advanced classifiers, e.g. random forests [67], or deep learning methods [68,69] could be used. A source of uncertainty in these segmentations as well as in the determination of indentation depth arise from image artefacts (e.g., rings, zingers, and beam hardening) that are present not only in the bulk material but also at the interface between air and indentation surface. The planar nature of this interface in combination with the diamond indenters led to artefacts in the phase contrast images. These artefacts were only

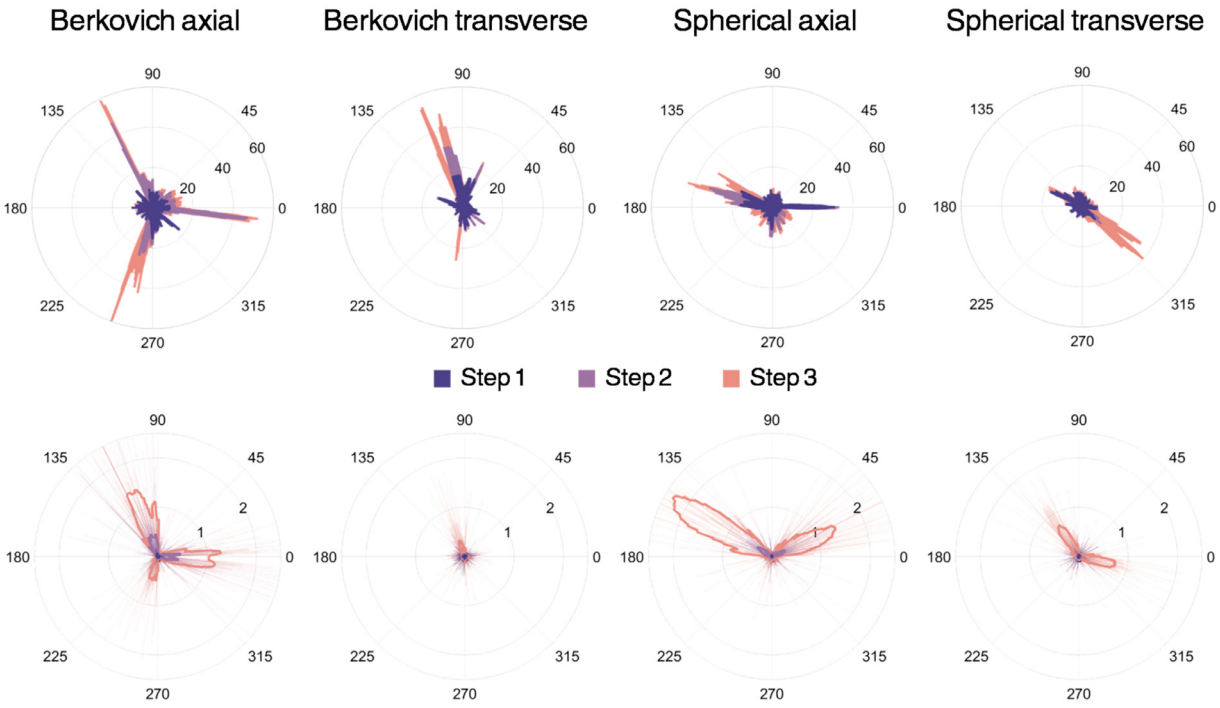

Fig. 6. Slice-wise polar plots of (top) crack volume and (bottom) hoop strains, ε_{φ}, computed using digital volume correlation at load steps 1 to 3 for four exemplary specimens displaying large radial cracks. For each angle, maximum values over the stack of slices are shown. The angular axis shows the angle in degrees, while crack volume in µm^3 and ε_{φ} in% are shown in the radial axis (top and bottom rows, respectively).

partially removed by smoothing and were accounted for by erosion and dilatation of the used masks. We believe this to be a robust approach in which information of a non-significant number of voxels at the indentation surface were lost.

There is a densified plastic zone under the indenter that induces a tensile stress state in the surrounding material. We observed a significantly spread tensile strain zone underneath the indenter from the beginning of our loading protocol that changed to a uniform compressive strain state with increasing distance from the indenter tip (Video 1, Video 2). A similar strain distribution has been observed beneath the indenters in ductile metals [70,71]. In addition, the residual strains reported by Karali et al. [25] in bovine cortical bone also showed an extensive residual tensile region under a Vickers indenter tip. However, compared to results from Karali et al. [25] we observed a more constrained and lower strained tensile region which may relate to the lower indentation depths we conducted and the higher resolution of both our image and DVC data, which led to more accurate and refined strain measurements. We did not observe significant strain heterogeneities within the tissue due to the presence of vascular or cellular porosity, which contradicts results reported in Christen et al. [32] for murine femurs, and may be explained by the different loading conditions, where the indentation loading we applied lead to a high deformation concentrated beneath the indenter tip. Furthermore, we observed strain magnitudes in excess of the 0.7% - 0.9% cortical bone yield strains previously reported [63,72,73] at load step 3 (Figs. 5, 6), confirming the extensive plastic deformation underneath the tip.

The tip geometry seemed to have little influence on the shape and size of the affected indentation volume. Nevertheless, spherical indentations led to larger strain values in both material directions, which may be due to the lack of self-similarity of the spherical indenter tip. The material anisotropy was also reflected by the larger strain accumulation in samples indented in the axial direction (Figs. 6, 7, Video 1, Video2), this difference is closely related to the fibrillar arrangement of bone extra cellular matrix in ovine cortical bone. As the femoral diaphysis is subjected to a significant bending moment during locomotion, the collagen fibrils are arranged to provide significant axial strength as well as resistance to crack propagation perpendicular to the length of the femur by deflecting those cracks towards the least load-bearing direction. Higher tensile hoop strains, indicating Mode I fracture, generally correlated with regions that display significant cracking radial to the indenter (Fig. 6). For transversely indented samples, as cracks are directed towards a plane that offer higher resistance to fracture, high radial strains accumulated in regions displaying cracking, which may indicate a change of fracture mode to shear (Mode II).

4.3. Local quantification of crack propagation

We used the displacement fields resulting from our DVC analysis to study the 3D opening of cracks propagating below the indenter tip. Christen et al. [32] analysed the crack opening displacements in notched mouse femurs subjected to compressive loading, however, the authors limited the displacement measurements to two-dimensional crack profiles. Here, we quantified the crack opening displacements in a 3D manner, which allowed us to infer not only the Mode I (opening) displacement, but also the shear (Mode II) and out-of-plane (Mode III) displacements (Fig. 7). While Mode III displacements were almost negligible, indentation loading with the Berkovich tip induced significant shear displacements in some of the analysed cracks, with magnitudes comparable to the Mode I displacements (Fig. 7, Figure S6). Similar observations were reported by Vertyagina et al. [29] in polycrystalline alumina beneath a Vickers indentation. Comparing the crack front profiles identified from our segmentation procedure against the crack opening displacement maps we showed that DVC is more sensitive that SRµCT in visualising the crack tip, as significant displacements are measured ahead of the identified front, indicating a process zone of high deformation. Indeed, DVC measures subpixel displacement, whereas µCT image contrast may not reliably detect crack opening lower than the image resolution [74]. In this

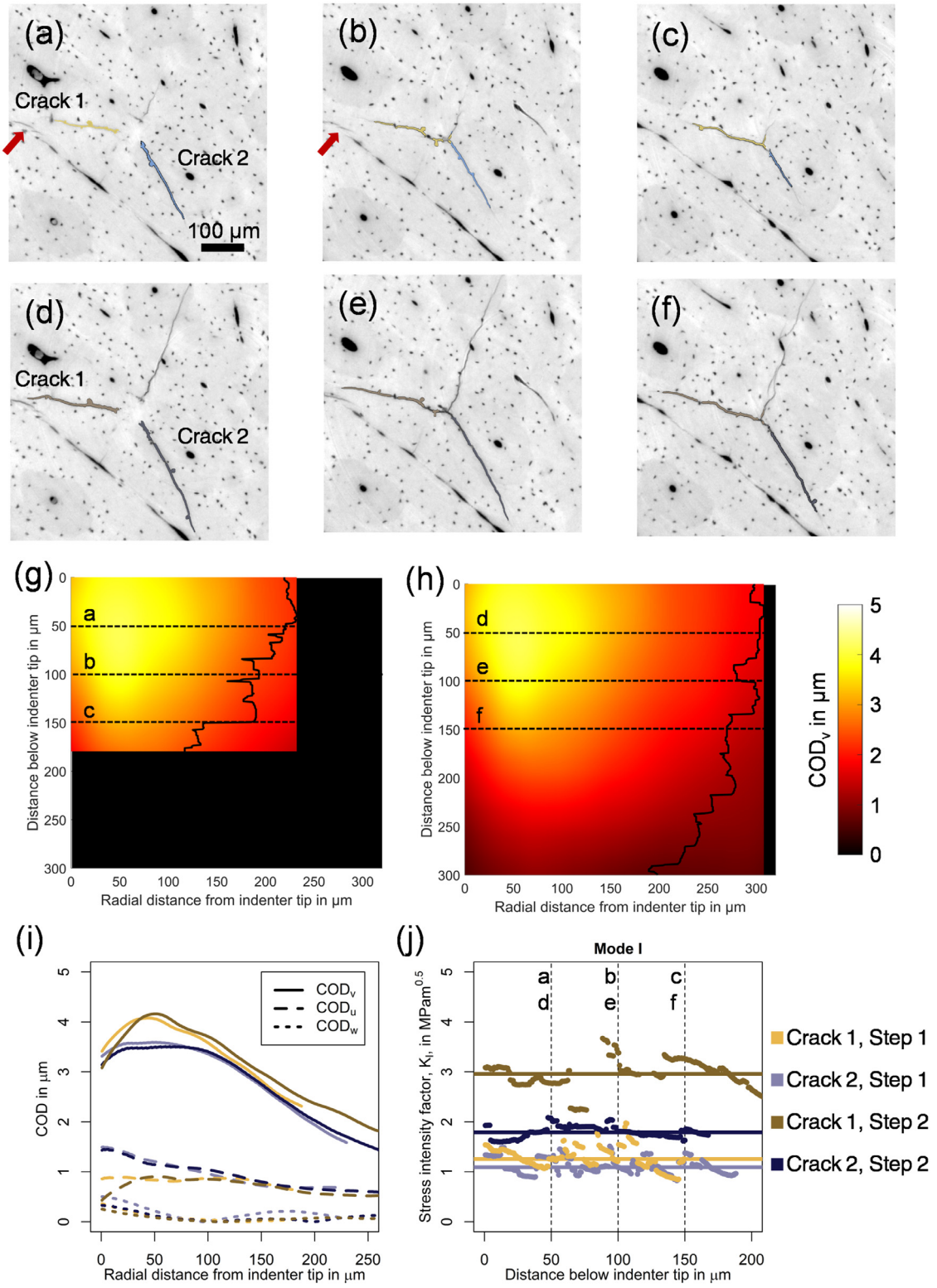

Fig. 7. Quantitative analysis of crack propagation during indentation loading. (a-f) SRµCT cross-section (a, d) 50 µm, (b, e) 100 µm, and (c, f) 150 µm below the Berkovich tip of a sample indented in the axial direction at (a-c) load step 2 and (d-f) load step 3 with the analysed microcracks coloured. Red arrows indicate pre-existing microdamage. (g, h) Crack opening displacements maps at (g) load step 2 and (h) load step 3 for the yellow/brown-coloured crack (Crack 1 in (a-f)). Dashed horizontal lines correspond to the planes depicted in (a, f). (i) Crack opening displacement profiles for microcracks highlighted in (b, e) 100 µm below the indenter tip. Mode I (COD_v), Mode II (COD_u), and Mode III (COD_w), opening displacements corresponding to pure opening, shear, and out of plane motion, are shown. (j) Mode I stress intensity factor (K_I) along the crack front. Horizontal lines represent mean K_I values along the crack front. Dashed vertical lines correspond to the planes depicted in (a-f). (For interpretation of the references to colour in this figure legend, the reader is referred to the web version of this article.)

perspective, phase congruency based algorithms might represent a better alternative to extract the crack tip position [75,76].

We found median Mode I opening displacements to increase only up to 1.93 µm, which is in line with reported measurements by Christen et al. [32], Hazenberg et al. [77] and Voide et al. [60]. Interestingly, when comparing the crack opening profiles at load steps 2 and 3 (Fig. 7), we observed that displacement magnitudes did not significantly increase when increasing the indentation load. Instead of increasing the crack opening displacement, energy is dissipated by either an increase of the crack length or the formation of new microcracks [32], due to the existence of uncracked ligament bridging in the intact bone mineral matrix, as well as collagen-fibril bridging in disrupted mineral matrix where the organic constituents are intact [64].

We extracted the stress intensity factor along the crack front using the 3D displacement fields from DVC following a similar approach as in Limodin et al. [37] and Toda et al. [35]. To the best of our knowledge, local stress intensity factor measurements have not been reported for bone tissue so far. While K_{III} values remained close to zero along the crack front of most of the cracks, some of the analysed cracks showed significant values of K_{II}, that cannot be neglected (Figure S6). However, Mode I was predominant, as expected from the prescribed loading conditions. K_I was observed to vary along the crack front (Fig. 7, Figure S6). This is a result of the complex crack geometry and propagation behaviour in cortical bone induced by indentation loading, and which may also be influenced by the type tissue (i.e., osteonal or interstitial) these cracks propagate through. Altogether, our results emphasize the importance of a 3D characterization of the fracture toughness, which may allow to correlate variations in local stress intensity factors with local material and/or microstructural changes.

Our measured K_I values are consistent with average bulk toughness measurements found in literature in ovine bone. Mullins et al. [22] reported values of 0.5 MPam$^{0.5}$ to 2.3 MPam$^{0.5}$ using cube corner indentation fracture test on samples orientated in the longitudinal (here called axial) direction, similar to our findings (Figure S6). They also align well with the stress intensity values of $\sim$ 1 MPam$^{0.5}$ to 2 MPam$^{0.5}$ reported by Koester et al. [52] in human cortical bone over the first 500 µm cracking in the longitudinal direction. Other studies, however, report crack initiation toughness in bovine cortical bone in the range of 2.2–5.2 MPam$^{0.5}$ [33,78–81] and 2.4–7.2 MPam$^{0.5}$ [80,82] in the transverse and longitudinal direction, respectively, using macroscale fracture mechanical testing. These are higher than the stress intensity fracture values we measured. This difference may be due to the short crack lengths and the absence of large crack deflections and twisting of the analysed cracks in our study (Fig. 4), but also the use of different fracture mechanics approaches. For instance, it was recently shown that traditional unloading compliance methods following the ASTM E1820 standard [83] underestimate crack extension, leading to significantly different fracture toughness measures compared to optical methods [84].

Bone tissue exhibits a rising fracture resistance with crack extension, thus, toughness measurements should be described as a function of crack extension [52,85]. Here, as cracks were barely detectable at load step 2, we were not able to analyse changes with increasing crack size. Yet, in one specimen, we observed an increase of K_I with increasing crack propagation (Fig. 7). As we restricted our analysis to cracks within our image field of view that propagated radially to the indentation axis based on our polar plots (Fig. 3), the number of cracks was rather limited, and we only analysed samples indented with the Berkovich tip in the axial direction. Therefore, we could not quantify differences between indenter geometry, either material orientation. While it is well known that the driving force for crack propagation is higher in the transverse direction than in the longitudinal direction [52,64], the complex crack growth pattern observed here, both axially and radially to the indentation axis, makes it difficult to assign an unique crack propagation direction to our specimens, for which traditional fracture toughness mechanical testing on compact-tension samples may be more appropriate.

To further validate our measurements, under small-scale yielding condition in Mode I, we can use the crack-tip opening displacements measured using DVC, which can be given in terms of the yield strength, σ_y, [86] by:

$$CTOD \approx \frac{4}{\pi}\frac{K_I^2}{\mu\sigma_y} \tag{4}$$

Considering our DVC-derived $CTOD$ and K_I, we obtain a mean ($\pm$ standard deviation) yield strength of 117 MPa ($\pm$ 65 MPa). These values align well with the strength measurements reported by Casari et al. [63] for dry ovine cortical bone at the length scale of multiple lamellae, where brittle failure was observed.

4.4. Irradiation-induced damage

An unexpected, yet most interesting result was the linear relaxation due to the X-ray beam (Fig. 1a). The effect of the X-ray beam on the stress-relaxation curves during *in situ* SRµCT experiments has been previously observed in bone [87] and soft tissues [88], however, to our knowledge, this behaviour has never been quantified. The relaxation was consistent throughout scanning, but its impact seems to have decreased towards the end of the loading protocol. This suggests that structures damaged by the beam were already largely broken in the later loading steps so that the relaxation decreased, in line with recent findings by Sauer et al. [89], who observed a decrease in the rate of relaxation of strains in prestressed hydroxyapatite crystals during *in situ* X-ray diffraction of dry bone specimens.

It is known that radiation is affecting the mechanical properties of bone [53,90–92] which complicates its use in *in situ* experiments. We, therefore, tried to minimise dose exposure minimising the exposure time. Since it has been proposed that X-rays affect the collagen network [53,54] which could, thus, lead to the observed effect, we investigated the composition using Raman microscopy. At first glance the results indicate indeed a significant difference in the amide I and II peaks between irradiated and non-irradiated samples (Figure S8) which would be in line with [53]. However, we observed a strong decrease in the signal-to-noise ratio in the irradiated specimens, suggesting that irradiation could alter the surface quality of the sample, thereby influencing the quality of the Raman spectra collected with small integration times. Based on our refined scans with significantly increased integration time and spectral resolution, it is evident that there are no clear changes between the peak shapes of the amide I and III peaks of irradiated and virgin material (Figure S9). The only difference that is visible is the decrease in signal-to-noise ratio for the irradiated sample due to increased background. This means that there are no clear changes in the protein α-helix, β-sheets and random coils (amide III) as well as in C==O bonds, immature cross-links, β-sheet and disordered secondary structure (amide I) on the molecular level [93]. Therefore, it seems that the collagen backbone and secondary structure are not strongly affected by the synchrotron irradiation, which contrasts the current state-of-knowledge [53]. The apparent embrittlement of the bone samples must therefore stem from changes in a different part of the organic phase, e.g., lipids or other non-collagenous proteins [93] visible in other smaller peaks within the Raman spectrum of bone. Due to the strong decrease in signal-to-noise ratio for the irradiated sample, these effects could not be verified experimentally in this study.

An alternative explanation of the linear relaxation and the sample embrittlement induced by the radiation could be damage to

the non-fibrillar organic matrix that bonds the mineralised fibrils and mineral particles, acting as a "glue" [94]. Destruction could be promoted by ionised water [95] or ionised calcium and phosphorous from the hydroxyapatite crystals [89] rupturing sacrificial bonds in the interfibrillar matrix of bone [94]. Instead of beam induced cross-linking reactions or fragmentation of collagen α-chains [53,96], these free radicals could physically disrupt the connectivity of the mineralised fibrils. This would destroy one of the toughening mechanisms that acts against crack growth in bone [97] and, consequently, lead to an increase of damage. This results then in an increase in compliance which, in turn, could explain the linear relaxation. Such a mechanism would not be detectable by our Raman spectroscopy measurements. While this mechanism could also be promoted by X-ray induced heating, the low thermal gradients previously measured during *in situ* SRμCT experiments [87] suggest that ionisation effects [89] may be more important.

4.5. Limitations of the study

We used cortical bone from ovine femur which has previously been found to be an acceptable model for human bone at the lamellar level [62,63]. However, ovine femoral bone is mostly primary bone and lacks cement line boundaries as compared with secondary compact bone [98,99]. The absence of cement sheaths results in the loss of one of the major extrinsic toughening mechanisms in bone: crack deflection and twisting at the cement lines [64]. As such, we did not observe major deflections as reported for human cortical bone [52], and most cracks penetrated the osteons. This allowed us to simply calculate crack opening displacements by taking two planes parallel to the main crack direction. However, this approach may not be feasible when cracks feature large local deflections, as expected when analysing secondary bone strained in the longitudinal direction. In such case, crack opening displacements will need to account for the local orientation of the cracks, and local stress intensities could be calculated by using crack-twist and crack-deflection mechanics [52].

Another limitation to be considered is the use of linear-elastic fracture mechanics (i.e., small-scale yielding conditions) to extract the stress intensity factors from the K-dominated field of the cracks of interest. Although linear-elastic fracture mechanics has been widely used to characterise bone toughness [78,80,100–104], the assumption that any inelastic behaviour is limited to a small near-tip region must be taken. As such, the stress intensity factors we report here do not account for the energy associated with plastic deformation during bone fracture, which relates to the intrinsic toughening in bone [64]. A nonlinear-elastic fracture mechanics approach using the J-Integral as the driving force for crack initiation and growth would be more appropriate to capture the contribution to the toughness from the elastic and plastic deformation. In this perspective, the DVC-measured displacements can be combined with finite element analysis to evaluate the J-integral and fracture toughness of the material of interest, as recently shown for trabecular bone in two-dimensions [105] and graphite in three dimensions [106]. This was, however, beyond the scope of this paper, where a fully experimental approach was considered. Nevertheless, the large experimental data we present here may serve to validate finite element models [107] that allows us to extract the yield properties of bone (e.g., yield stress and hardening exponent) using inverse methods from the DVC-measured deformation field [70], as well as phase-field fracture models [108] to analyse the fracture behaviour of cortical bone.

A further limitation of this study is the fact that the specimens were subjected to SR X-ray radiation, as discussed in Section 4.4. Whilst we did not directly measure the radiation dose absorbed by our samples, we can provide an estimate based on previous literature. Pacureanu et al. [109] reported radiation flux density of 1.9×10^{13} photon/s/cm^2 in beamline ID19 using the same insertion device. Considering the cylindrical geometry of our bone samples, with an apparent density of 1.5 g/cm^3 [110] and a mass attenuation coefficient of 1.26 cm^2/g at 31 keV [111], we could estimate the dose rate following [91] as 93.9 Gy/s, which results in a total dose of 28.2 kGy per tomogram and 112.6 kGy for the four loading steps considered in our crack propagation, deformation, and fracture analysis. However, the estimation of the flux density in Pacureanu et al. [109] was done for a lower energy and higher resolution compared to our study (19 keV and 0.3 μm voxel size, respectively). Suuronen et al. [112] reported relative dose at 29.6 keV is only ~70% of that incurred when at 17.5 keV, while Immel et al. [113] described an exponential relationship between radiation dose and image resolution. Moreover, we did not consider the flux attenuation introduced by the filters and micromechanical device [91]. Altogether, it is likely that the total radiation dose absorbed by our samples was significantly lower than 100 kGy, yet above the suggested 'safe' threshold of 35 kGy [53]. Low-dose high-resolution SR imaging remains challenging, and while optimisation of imaging setup [87,91] and reconstruction approaches using, for example, deep learning [33] are being developped, future work is needed to assess whether the accuracy of DVC based on deep learning generated images will hold. Still, we show a clear effect of the X-ray beam on the stress relaxation behaviour of our specimens from the beginning of our loading protocol. In addition, it has been recently suggested that there is likely no truly safe dose for bone material, as radiation damage in bone is not strictly dose-dependant [89]. Therefore, we believe that further studies could help to decipher the mechanisms behind the observed sample embrittlement and the implications on the measured mechanical properties across length-scales.

5. Conclusion

We characterised the crack propagation, deformation, and fracture behaviour of ovine cortical bone under Berkovich and spherical indenter tips using *in situ* high-resolution SRμCT and DVC. Our results highlight the structural anisotropy of bone, with lower strains and smaller crack systems developing in samples indented in the transverse direction, independently of the indenter type. Cracking in the radial direction was correlated with high tensile hoop strains, suggesting that tensile hoop stress serve to open microcracks. The 3D nature of the DVC data allowed us to provide a local quantification of the crack propagation behaviour, where crack opening displacements and stress intensity factors were evaluated from the full displacement field underneath the indenter tip, indicating a predominant Mode I fracture mode, however, Mode II fracture (i.e., shear) was also present. Analyses of the beam impact revealed no damage in the collagen backbone and secondary structure which contrasts the current state-of-knowledge. However, other organic structures inside the extracellular matrix like collagen cross-links, lipids, or other non-collagenous proteins might be affected. Beam induced relaxation data indicates that the beam impact could be linked to an embrittlement process that may affect the non-fibrillar organic bone matrix. The experimental data and methodology we present here will improve our understanding of indentation tests and their results and will serve to implement and validate finite element models that allow us to evaluate the elastic, yield, and fracture properties of bone. This will favour the analysis of bone failure mechanisms and bone fracture resistance in relation to structural and material changes due to ageing or disease. Ultimately, assessing how differences in bone extracellular matrix, bone mineral content and bone microstructure influence the resistance to crack propagation in bone may enable the development of treatment strategies that prevent bone fracture.

Declaration of competing interest

The authors declare that they have no known competing financial interests or personal relationships that could have appeared to influence the work reported in this paper.

Acknowledgments

The project was supported by a Leverhulme Research Project Grant to U.W. (RPG-2020-215), the AO Foundation (AO S-12-13W) and the LabEx PRIMES framework (ANR-11-LABX-006) of Université de Lyon. We would like to thank the ESRF for providing beam-time within LTP MD431, James Best for his assistance with Raman analysis, and Max Langer and Loriane Weber for help during the experiment. Finally, we would like to thank the team of the ARTORG workshop around Urs Rohrer for manufacturing the devices for the project.

Supplementary materials

Supplementary material associated with this article can be found, in the online version, at doi:10.1016/j.actbio.2023.04.038.

References

[1] P. Fratzl, R. Weinkamer, Nature's hierarchical materials, Prog. Mater. Sci. 52 (2007) 1263–1334, doi:10.1016/j.pmatsci.2007.06.001.
[2] P. Augat, S. Schorlemmer, The role of cortical bone and its microstructure in bone strength, Age Ageing 35 (2006) 27–31, doi:10.1093/ageing/afl081.
[3] S. Weiner, W. Traub, H.D. Wagner, Lamellar bone: structure– function relations, J. Struct. Biol. 126 (1999) 241–255.
[4] N. Reznikov, R. Shahar, S. Weiner, Three-dimensional structure of human lamellar bone: the presence of two different materials and new insights into the hierarchical organization, Bone 59 (2014) 93–104, doi:10.1016/j.bone.2013.10.023.
[5] P. Varga, A. Pacureanu, M. Langer, H. Suhonen, B. Hesse, Q. Grimal, P. Cloetens, K. Raum, F. Peyrin, Investigation of the three-dimensional orientation of mineralized collagen fibrils in human lamellar bone using synchrotron X-ray phase nano-tomography, Acta Biomater 9 (2013) 8118–8127, doi:10.1016/j.actbio.2013.05.015.
[6] P. Zioupos, M. Gresle, K. Winwood, Fatigue strength of human cortical bone: age, physical, and material heterogeneity effects, J. Biomed. Mater. Res. Part A. 86 (2008) 627–636, doi:10.1002/jbm.a.31576.
[7] P. Zioupos, J.D. Currey, Changes in the stiffness, strength, and toughness of human cortical bone with age, Bone 22 (1998) 57–66, doi:10.1016/S8756-3282(97)00228-7.
[8] R.K. Nalla, J.J. Kruzic, J.H. Kinney, R.O. Ritchie, Effect of aging on the toughness of human cortical bone: evaluation by R-curves, Bone 35 (2004) 1240–1246, doi:10.1016/j.bone.2004.07.016.
[9] M.J. Mirzaali, J.J. Schwiedrzik, S. Thaiwichai, J.P. Best, J. Michler, P.K. Zysset, U. Wolfram, Mechanical properties of cortical bone and their relationships with age, gender, composition and microindentation properties in the elderly, Bone 93 (2016) 196–211, doi:10.1016/j.bone.2015.11.018.
[10] G. Osterhoff, E.F. Morgan, S.J. Shefelbine, L. Karim, L.M. McNamara, P. Augat, Bone mechanical properties and changes with osteoporosis, Injury 47 (2016) S11–S20, doi:10.1016/S0020-1383(16)47003-8.
[11] P.K. Zysset, Indentation of bone tissue: a short review, Osteoporos. Int. 20 (2009) 1049–1055, doi:10.1007/s00198-009-0854-9.
[12] W.C. Oliver, G.M. Pharr, Measurement of hardness and elastic modulus by instrumented indentation: advances in understanding and refinements to methodology, J. Mater. Res. 19 (2004) 3–20, doi:10.1557/jmr.2004.19.1.3.
[13] K. Tai, F.J. Ulm, C. Ortiz, Nanogranular origins of the strength of bone, Nano Lett 6 (2006) 2520–2525, doi:10.1021/nl061877k.
[14] L.P. Mullins, M.S. Bruzzi, P.E. McHugh, Calibration of a constitutive model for the post-yield behaviour of cortical bone, J. Mech. Behav. Biomed. Mater. 2 (2009) 460–470, doi:10.1016/j.jmbbm.2008.11.003.
[15] J.J. Schwiedrzik, P.K. Zysset, The influence of yield surface shape and damage in the depth-dependent response of bone tissue to nanoindentation using spherical and Berkovich indenters, Comput. Methods Biomech. Biomed. Eng. 18 (2015) 492–505, doi:10.1080/10255842.2013.818665.
[16] C. Renteria, J.M. Fernández-Arteaga, J. Grimm, E.A. Ossa, D. Arola, Mammalian enamel: a universal tissue and diverse source of inspiration, Acta Biomater. 136 (2021) 402–411, doi:10.1016/j.actbio.2021.09.016.
[17] S. Amini, A. Masic, L. Bertinetti, J.S. Teguh, J.S. Herrin, X. Zhu, H. Su, A. Miserez, Textured fluorapatite bonded to calcium sulphate strengthen stomatopod raptorial appendages, Nat. Commun. 5 (2014), doi:10.1038/ncomms4187.
[18] A. Miserez, J.C. Weaver, P.J. Thurner, J. Aizenberg, Y. Dauphin, P. Fratzl, D.E. Morse, F.W. Zok, Effects of laminate architecture on fracture resistance of sponge biosilica: lessons from nature, Adv. Funct. Mater. 18 (2008) 1241–1248, doi:10.1002/adfm.200701135.
[19] Z. Deng, H.C. Loh, Z. Jia, C.A. Stifler, A. Masic, P.U.P.A. Gilbert, R. Shahar, L. Li, Black drum fish teeth: built for crushing mollusk shells, Acta Biomater. 137 (2022) 147–161, doi:10.1016/j.actbio.2021.10.023.
[20] M.A. Marcus, S. Amini, C.A. Stifler, C.Y. Sun, N. Tamura, H.A. Bechtel, D.Y. Parkinson, H.S. Barnard, X.X.X. Zhang, J.Q.I. Chua, A. Miserez, P.U.P.A. Gilbert, Parrotfish teeth: stiff biominerals whose microstructure makes them tough and abrasion-resistant to bite stony corals, ACS Nano 11 (2017) 11856–11865, doi:10.1021/acsnano.7b05044.
[21] L. Kundanati, M. D'Incau, M. Bernardi, P. Scardi, N.M. Pugno, A comparative study of the mechanical properties of a dinosaur and crocodile fossil teeth, J. Mech. Behav. Biomed. Mater. 97 (2019) 365–374, doi:10.1016/j.jmbbm.2019.05.025.
[22] L.P. Mullins, M.S. Bruzzi, P.E. McHugh, Measurement of the microstructural fracture toughness of cortical bone using indentation fracture, J. Biomech. 40 (2007) 3285–3288, doi:10.1016/j.jbiomech.2007.04.020.
[23] J.J. Kruzic, D.K. Kim, K.J. Koester, R.O. Ritchie, Indentation techniques for evaluating the fracture toughness of biomaterials and hard tissues, J. Mech. Behav. Biomed. Mater. 2 (2009) 384–395, doi:10.1016/j.jmbbm.2008.10.008.
[24] R.M. Hoerth, M. Kerschnitzki, M. Aido, I. Schmidt, M. Burghammer, G.N. Duda, P. Fratzl, B.M. Willie, W. Wagermaier, Correlations between nanostructure and micromechanical properties of healing bone, J. Mech. Behav. Biomed. Mater. 77 (2018) 258–266, doi:10.1016/j.jmbbm.2017.08.022.
[25] A. Karali, A.P. Kao, J. Zekonyte, G. Blunn, G. Tozzi, Micromechanical evaluation of cortical bone using in situ XCT indentation and digital volume correlation, J. Mech. Behav. Biomed. Mater. 115 (2021) 104298, doi:10.1016/j.jmbbm.2020.104298.
[26] T. Lowe, E. Avcu, E. Bousser, W. Sellers, P.J. Withers, 3D Imaging of indentation damage in bone, Materials (Basel) 11 (2018) 1–13, doi:10.3390/ma11122533.
[27] X. Lu, M.P. Fernández, R.S. Bradley, S.D. Rawson, M. O'Brien, B. Hornberger, M. Leibowitz, G. Tozzi, P.J. Withers, Anisotropic crack propagation and deformation in dentin observed by four-dimensional X-ray nano-computed tomography, Acta Biomater. 96 (2019) 400–411, doi:10.1016/j.actbio.2019.06.042.
[28] T. Lacondemine, J. Réthoré, É. Maire, F. Célarié, P. Houizot, C. Roux-Langlois, C.M. Schlepütz, T. Rouxel, Direct observation of the displacement field and microcracking in a glass by means of X-ray tomography during in situ Vickers indentation experiment, Acta Mater. 179 (2019) 424–433, doi:10.1016/j.actamat.2019.07.053.
[29] Y. Vertyagina, M. Mostafavi, C. Reinhard, R. Atwood, T.J. Marrow, In situ quantitative three-dimensional characterisation of sub-indentation cracking in polycrystalline alumina, J. Eur. Ceram. Soc. 34 (2014) 3127–3132, doi:10.1016/j.jeurceramsoc.2014.04.002.
[30] M. Peña Fernández, A.P. Kao, R. Bonithon, D. Howells, A.J. Bodey, K. Wanelik, F. Witte, R. Johnston, H. Arora, G. Tozzi, Time-resolved in situ synchrotron-microCT: 4D deformation of bone and bone analogues using digital volume correlation, Acta Biomater. 131 (2021) 424–439, doi:10.1016/j.actbio.2021.06.014.
[31] M. Peña Fernández, A.P. Kao, F. Witte, H. Arora, G. Tozzi, Low-cycle full-field residual strains in cortical bone and their influence on tissue fracture evaluated via in situ stepwise and continuous X-ray computed tomography, J. Biomech. 113 (2020) 110105, doi:10.1016/j.jbiomech.2020.110105.
[32] D. Christen, A. Levchuk, S. Schori, P. Schneider, S.K. Boyd, R. Müller, Deformable image registration and 3D strain mapping for the quantitative assessment of cortical bone microdamage, J. Mech. Behav. Biomed. Mater. 8 (2012) 184–193, doi:10.1016/j.jmbbm.2011.12.009.
[33] M. Sieverts, Y. Obata, J.L. Rosenberg, W. Woolley, D.Y. Parkinson, H.S. Barnard, D.M. Pelt, C. Acevedo, Unraveling the effect of collagen damage on bone fracture using in situ synchrotron microtomography with deep learning, Commun. Mater. 3 (2022) 78, doi:10.1038/s43246-022-00296-6.
[34] E. Dall'Ara, M. Peña-Fernández, M. Palanca, M. Giorgi, L. Cristofolini, G. Tozzi, Precision of digital volume correlation approaches for strain analysis in bone imaged with micro-computed tomography at different dimensional levels, Front. Mater. 4 (2017), doi:10.3389/fmats.2017.00031.
[35] H. Toda, E. Maire, S. Yamauchi, H. Tsuruta, T. Hiramatsu, M. Kobayashi, In situ observation of ductile fracture using X-ray tomography technique, Acta Mater. 59 (2011) 1995–2008, doi:10.1016/j.actamat.2010.11.065.
[36] N. Limodin, J. Réthoré, J.-Y. Buffière, F. Hild, W. Ludwig, J. Rannou, S. Roux, 3D X-ray microtomography volume correlation to study fatigue crack growth, Adv. Eng. Mater. 13 (2011) 186–193, doi:10.1002/adem.201000235.
[37] N. Limodin, J. Réthoré, J.Y. Buffière, A. Gravouil, F. Hild, S. Roux, Crack closure and stress intensity factor measurements in nodular graphite cast iron using three-dimensional correlation of laboratory X-ray microtomography images, Acta Mater. 57 (2009) 4090–4101, doi:10.1016/j.actamat.2009.05.005.
[38] J.C. Labiche, O. Mathon, S. Pascarelli, M.A. Newton, G.G. Ferre, C. Curfs, G. Vaughan, A. Homs, D.F. Carreiras, Invited article: the fast readout low noise camera as a versatile x-ray detector for time resolved dispersive extended x-ray absorption fine structure and diffraction studies of dynamic problems in materials science, chemistry, and catalysis, Rev. Sci. Instrum. (2007) 78, doi:10.1063/1.2783112.
[39] P.-A. Douissard, A. Cecilia, X. Rochet, X. Chapel, T. Martin, T. van de Kamp, L. Helfen, T. Baumbach, L. Luquot, X. Xiao, J. Meinhardt, A. Rack, A versatile indirect detector design for hard X-ray microimaging, J. Instrum. 7 (2012) 9016, doi:10.1088/1748-0221/7/09/P09016.
[40] D. Paganin, S.C. Mayo, T.E. Gureyev, P.R. Miller, S.W. Wilkins, Simultaneous phase and amplitude extraction from a single defocused image of a homogeneous object, J. Microsc. 206 (2002) 33–40, doi:10.1046/j.1365-2818.2002.01010.x.

[41] A. Mirone, E. Brun, E. Gouillart, P. Tafforeau, J. Kieffer, The PyHST2 hybrid distributed code for high speed tomographic reconstruction with iterative reconstruction and a priori knowledge capabilities, Nucl. Instruments Methods Phys. Res. Sect. 324 (2014) 41–48, doi:10.1016/j.nimb.2013.09.030.
[42] A. Lyckegaard, G. Johnson, P. Tafforeau, Correction of ring artifacts in X-ray tomographic images, Int. J. Tomogr. Stat. 18 (2011) 1–9.
[43] B.C. Lowekamp, D.T. Chen, L. Ibáñez, D. Blezek, The design of SimpleITK, Front. Neuroinform. 7 (2013) 45, doi:10.3389/fninf.2013.00045.
[44] K.J. Millman, M. Aivazis, Python for Scientists and Engineers, 2007, pp. 9–12.
[45] T.S. Yoo, M.J. Ackerman, W.E. Lorensen, W. Schroeder, V. Chalana, S. Aylward, D. Metaxas, R. Whitaker, Engineering and algorithm design for an image processing Api: a technical report on ITK–the Insight Toolkit, Stud. Health Technol. Inform. 85 (2002) 586–592.
[46] A.C. Fischer-Cripps, Nanoindentation (2004), doi:10.1007/978-1-4757-5943-3.
[47] F. Gillard, R. Boardman, M. Mavrogordato, D. Hollis, I. Sinclair, F. Pierron, M. Browne, The application of digital volume correlation (DVC) to study the microstructural behaviour of trabecular bone during compression, J. Mech. Behav. Biomed. Mater. 29 (2014) 480–499, doi:10.1016/j.jmbbm.2013.09.014.
[48] M. Peña Fernández, A.H. Barber, G.W. Blunn, G. Tozzi, Optimization of digital volume correlation computation in SR-microCT images of trabecular bone and bone-biomaterial systems, J. Microsc. 272 (2018) 213–228, doi:10.1111/jmi.12745.
[49] L. Liu, E.F. Morgan, Accuracy and precision of digital volume correlation in quantifying displacements and strains in trabecular bone, J. Biomech. 40 (2007) 3516–3520, doi:10.1016/j.jbiomech.2007.04.019.
[50] M. Palanca, G. Tozzi, L. Cristofolini, M. Viceconti, E. Dall'Ara, Three-dimensional local measurements of bone strain and displacement: comparison of three digital volume correlation approaches, J. Biomech. Eng. 137 (2015) 1–14, doi:10.1115/1.4030174.
[51] M.L. Williams, The bending stress distribution at the base of a stationary crack, J. Appl. Mech. Trans. ASME. 28 (1960) 78–82, doi:10.1115/1.3640470.
[52] K.J. Koester, J.W. Ager, R.O. Ritchie, The true toughness of human cortical bone measured with realistically short cracks, Nat. Mater. 7 (2008) 672–677, doi:10.1038/nmat2221.
[53] H.D. Barth, M.E. Launey, A.A. MacDowell, J.W. Ager, R.O. Ritchie, On the effect of X-ray irradiation on the deformation and fracture behavior of human cortical bone, Bone 46 (2010) 1475–1485, doi:10.1016/j.bone.2010.02.025.
[54] H.D. Barth, E.A. Zimmermann, E. Schaible, S.Y. Tang, T. Alliston, R.O. Ritchie, Characterization of the effects of x-ray irradiation on the hierarchical structure and mechanical properties of human cortical bone, Biomaterials 32 (2011) 8892–8904, doi:10.1016/j.biomaterials.2011.08.013.
[55] G.R. Irwin, Analysis of stresses and strains near the end of a crack traversing a plate, J. Appl. Mech. 24 (1957) 361–364, doi:10.1115/1.4011547.
[56] R.O. Ritchie, D. Liu, Linear-elastic fracture mechanics (LEFM), 2021. 10.1016/b978-0-323-89822-5.00007-4.
[57] T.M. James, M. Schlösser, R.J. Lewis, S. Fischer, B. Bornschein, H.H. Telle, Automated quantitative spectroscopic analysis combining background subtraction, cosmic ray removal, and peak fitting, Appl. Spectrosc. 67 (2013) 949–959, doi:10.1366/12-06766.
[58] M.J. Crawley, Statistics: An Introduction Using R, 2nd ed., Wiley, 2014.
[59] P.J. Thurner, P. Wyss, R. Voide, M. Stauber, M. Stampanoni, U. Sennhauser, R. Müller, Time-lapsed investigation of three-dimensional failure and damage accumulation in trabecular bone using synchrotron light, Bone 39 (2006) 289–299, doi:10.1016/j.bone.2006.01.147.
[60] R. Voide, P. Schneider, M. Stauber, P. Wyss, M. Stampanoni, U. Sennhauser, G.H. van Lenthe, R. Müller, Time-lapsed assessment of microcrack initiation and propagation in murine cortical bone at submicrometer resolution, Bone 45 (2009) 164–173, doi:10.1016/j.bone.2009.04.248.
[61] M. Peña Fernández, E. Dall'Ara, A.J. Bodey, R. Parwani, A.H. Barber, G.W. Blunn, G. Tozzi, E. Dall'Ara, A.J. Bodey, R. Parwani, A.H. Barber, G.W. Blunn, G. Tozzi, Full-field strain analysis of bone–biomaterial systems produced by the implantation of osteoregenerative biomaterials in an ovine model, ACS Biomater. Sci. Eng. 5 (2019) 2543–2554, doi:10.1021/acsbiomaterials.8b01044.
[62] J. Schwiedrzik, R. Raghavan, A. Bürki, V. LeNader, U. Wolfram, J. Michler, P. Zysset, In situ micropillar compression reveals superior strength and ductility but an absence of damage in lamellar bone, Nat. Mater. 13 (2014) 740, doi:10.1038/nmat3959.
[63] D. Casari, J. Michler, P. Zysset, J. Schwiedrzik, Microtensile properties and failure mechanisms of cortical bone at the lamellar level, Acta Biomater. 120 (2021) 135–145, doi:10.1016/j.actbio.2020.04.030.
[64] M.E. Launey, M.J. Buehler, R.O. Ritchie, On the mechanistic origins of toughness in bone, Annu. Rev. Mater. Res. 40 (2010) 25–53, doi:10.1146/annurev-matsci-070909-104427.
[65] U. Wolfram, J.J. Schwiedrzik, M.J. Mirzaali, A. BÜRKI, P. Varga, C. Olivier, F. Peyrin, P.K. Zysset, Characterizing microcrack orientation distribution functions in osteonal bone samples, J. Microsc. 264 (2016) 268–281, doi:10.1111/jmi.12440.
[66] F.J. O'Brien, D. Taylor, T.Clive Lee, Bone as a composite material: the role of osteons as barriers to crack growth in compact bone, Int. J. Fatigue. 29 (2007) 1051–1056, doi:10.1016/j.ijfatigue.2006.09.017.
[67] Y. Shi, L. Cui, Z. Qi, F. Meng, Z. Chen, Automatic road crack detection using random structured forests, IEEE Trans. Intell. Transp. Syst. 17 (2016) 1–12.
[68] T. Strohmann, K. Bugelnig, E. Breitbarth, F. Wilde, T. Steffens, H. Germann, G. Requena, Semantic segmentation of synchrotron tomography of multiphase Al-Si alloys using a convolutional neural network with a pixel-wise weighted loss function, Sci. Rep. 9 (2019) 1–9, doi:10.1038/s41598-019-56008-7.
[69] C. Xiao, J.Y. Buffiere, Neural network segmentation methods for fatigue crack images obtained with X-ray tomography, Eng. Fract. Mech. 252 (2021), doi:10.1016/j.engfracmech.2021.107823.
[70] M. Mostafavi, D.M. Collins, B. Cai, R. Bradley, R.C. Atwood, C. Reinhard, X. Jiang, M. Galano, P.D. Lee, T.J. Marrow, Yield behavior beneath hardness indentations in ductile metals, measured by three-dimensional computed X-ray tomography and digital volume correlation, Acta Mater. 82 (2015) 468–482, doi:10.1016/j.actamat.2014.08.046.
[71] B. Cai, P.D. Lee, S. Karagadde, T.J. Marrow, T. Connolley, Time-resolved synchrotron tomographic quantification of deformation during indentation of an equiaxed semi-solid granular alloy, Acta Mater. 105 (2016) 338–346, doi:10.1016/j.actamat.2015.11.028.
[72] H.H. Bayraktar, E.F. Morgan, G.L. Niebur, G.E. Morris, E.K. Wong, T.M. Keaveny, Comparison of the elastic and yield properties of human femoral trabecular and cortical bone tissue, J. Biomech. 37 (2004) 27–35, doi:10.1016/S0021-9290(03)00257-4.
[73] J. Schwiedrzik, A. Taylor, D. Casari, U. Wolfram, P. Zysset, J. Michler, Nanoscale deformation mechanisms and yield properties of hydrated bone extracellular matrix, Acta Biomater 60 (2017) 302–314, doi:10.1016/j.actbio.2017.07.030.
[74] M. Mostafavi, S.A. McDonald, P.M. Mummery, T.J. Marrow, Observation and quantification of three-dimensional crack propagation in poly-granular graphite, Eng. Fract. Mech. 110 (2013) 410–420, doi:10.1016/j.engfracmech.2012.11.023.
[75] A.F. Cinar, S.M. Barhli, D. Hollis, M. Flansbjer, R.A. Tomlinson, T.J. Marrow, M. Mostafavi, An autonomous surface discontinuity detection and quantification method by digital image correlation and phase congruency, Opt. Lasers Eng. 96 (2017) 94–106, doi:10.1016/j.optlaseng.2017.04.010.
[76] X. Jin, J. Wade-Zhu, Y. Chen, P.M. Mummery, X. Fan, T.J. Marrow, Assessment of the fracture toughness of neutron-irradiated nuclear graphite by 3D analysis of the crack displacement field, Carbon 171 (2021) 882–893, doi:10.1016/j.carbon.2020.09.072.
[77] J.G. Hazenberg, D. Taylor, T.Clive Lee, Mechanisms of short crack growth at constant stress in bone, Biomaterials 27 (2006) 2114–2122, doi:10.1016/j.biomaterials.2005.09.039.
[78] P. Lucksanasombool, W.A.J. Higgs, R.J.E.. Higgs, M.V. Swain, Fracture toughness of bovine bone: influence of orientation and storage media, Biomaterials 22 (2001) 3127–3132, doi:10.1016/S0142-9612(01)00062-X.
[79] G. Pezzotti, S. Sakakura, Study of the toughening mechanisms in bone and biomimetic hydroxyapatite materials using Raman microprobe spectroscopy, J. Biomed. Mater. Res. Part A. 65A (2003) 229–236, doi:10.1002/jbm.a.10447.
[80] W. Bonfield, M.D. Grynpas, R.J. Young, Crack velocity and the fracture of bone, J. Biomech. 11 (1978) 473–479, doi:10.1016/0021-9290(78)90058-1.
[81] T.M. Wright, W.C. Hayes, Fracture mechanics parameters for compact bone-Effects of density and specimen thickness, J. Biomech. 10 (1977), doi:10.1016/0021-9290(77)90019-7.
[82] T.L. Norman, D. Vashishth, D.B. Burr, Effect of groove on bone fracture toughness, J. Biomech. 25 (1992) 1489–1492, doi:10.1016/0021-9290(92)90061-5.
[83] ASTM Standard E1820-13, Standard test method for measurement of fracture toughness, ASTM B Stand. (2015) 1–54, doi:10.1520/E1820-13.
[84] D. Dapaah, T. Willett, A critical evaluation of cortical bone fracture toughness testing methods, J. Mech. Behav. Biomed. Mater. 134 (2022) 105419, doi:10.1016/j.jmbbm.2022.105419.
[85] R.K. Nalla, J.J. Kruzic, J.H. Kinney, R.O. Ritchie, Mechanistic aspects of fracture and R-curve behavior in human cortical bone, Biomaterials 26 (2005) 217–231, doi:10.1016/j.biomaterials.2004.02.017.
[86] R.O. Ritchie, D. Liu, Crack-tip opening displacement (CTOD), Introd. to Fract. Mech., 75–80, Elsevier, 2021, doi:10.1016/B978-0-323-89822-5.00002-5.
[87] M. Peña Fernández, E. Dall'Ara, A.P. Kao, A.J. Bodey, A. Karali, G.W. Blunn, A.H. Barber, G. Tozzi, Preservation of bone tissue integrity with temperature control for in situ SR-MicroCT experiments, Materials 11 (2018) 2155, doi:10.3390/ma11112155.
[88] C.M. Disney, A. Eckersley, J.C. McConnell, H. Geng, A.J. Bodey, J.A. Hoyland, P.D. Lee, M.J. Sherratt, B.K. Bay, Synchrotron tomography of intervertebral disc deformation quantified by digital volume correlation reveals microstructural influence on strain patterns, Acta Biomater 92 (2019) 290–304, doi:10.1016/j.actbio.2019.05.021.
[89] K. Sauer, I. Zizak, J.B. Forien, A. Rack, E. Scoppola, P. Zaslansky, Primary radiation damage in bone evolves via collagen destruction by photoelectrons and secondary emission self-absorption, Nat. Commun. 13 (2022) 7829, doi:10.1038/s41467-022-34247-z.
[90] J.D. Currey, J. Foreman, I. Laketić, J. Mitchell, D.E. Pegg, G.C. Reilly, Effects of ionizing radiation on the mechanical properties of human bone, J. Orthop. Res. 15 (1997) 111–117, doi:10.1002/jor.1100150116.
[91] M. Peña Fernández, S. Cipiccia, E. Dall'Ara, A.J. Bodey, R. Parwani, M. Pani, G.W. Blunn, A.H. Barber, G. Tozzi, Effect of SR-microCT radiation on the mechanical integrity of trabecular bone using in situ mechanical testing and digital volume correlation, J. Mech. Behav. Biomed. Mater. 88 (2018) 109–119, doi:10.1016/j.jmbbm.2018.08.012.
[92] F.N. Schmidt, M. Hahn, K.E. Stockhausen, T. Rolvien, C. Schmidt, T. Knopp, C. Schulze, K. Püschel, M. Amling, B. Busse, Influence of X-rays and gamma-rays on the mechanical performance of human bone factoring out intraindividual bone structure and composition indices, Mater. Today Bio. 13 (2022), doi:10.1016/j.mtbio.2021.100169.

[93] G.S. Mandair, M.D. Morris, Contributions of Raman spectroscopy to the understanding of bone strength, Bonekey Rep. 4 (2015) 1–8, doi:10.1038/bonekey.2014.115.
[94] G.E. Fantner, T. Hassenkam, J.H. Kindt, J.C. Weaver, H. Birkedal, L. Pechenik, J.A. Cutroni, G.A.G. Cidade, G.D. Stucky, D.E. Morse, P.K. Hansma, Sacrificial bonds and hidden length dissipate energy as mineralized fibrils separate during bone fracture, Nat. Mater. 4 (2005) 612–616, doi:10.1038/nmat1428.
[95] O. Akkus, R.M. Belaney, P. Das, Free radical scavenging alleviates the biomechanical impairment of gamma radiation sterilized bone tissue, J. Orthop. Res. 23 (2005) 838–845, doi:10.1016/j.orthres.2005.01.007.
[96] B. Burton, A. Gaspar, D. Josey, J. Tupy, M.D. Grynpas, T.L. Willett, Bone embrittlement and collagen modifications due to high-dose gamma-irradiation sterilization, Bone 61 (2014) 71–81, doi:10.1016/j.bone.2014.01.006.
[97] A.A. Poundarik, T. Diab, G.E. Sroga, A. Ural, A.L. Boskey, C.M. Gundberg, D. Vashishth, Dilatational band formation in bone, Proc. Natl. Acad. Sci. U. S. A. 109 (2012) 19178–19183, doi:10.1073/pnas.1201513109.
[98] S. Mohsin, F.J. O'Brien, T.C. Lee, Osteonal crack barriers in ovine compact bone, J. Anat. 208 (2006) 81–89, doi:10.1111/j.1469-7580.2006.00509.x.
[99] M.L. Hillier, L.S. Bell, Differentiating human bone from animal bone: a review of histological methods, J. Forensic Sci. 52 (2007) 249–263, doi:10.1111/j.1556-4029.2006.00368.x.
[100] J.B. Phelps, G.B. Hubbard, X. Wang, C.M. Agrawal, Microstructural heterogeneity and the fracture toughness of bone, J. Biomed. Mater. Res. 51 (2000) 735–741, doi:10.1002/1097-4636(20000915)51:4<735::AID-JBM23>3.0.CO;2-G.
[101] X.D. Wang, N.S. Masilamani, J.D. Mabrey, M.E. Alder, C.M. Agrawal, Changes in the fracture toughness of bone may not be reflected in its mineral density, porosity, and tensile properties, Bone 23 (1998) 67–72, doi:10.1016/S8756-3282(98)00071-4.
[102] O. Akkus, F. Adar, M.B. Schaffler, Age-related changes in physicochemical properties of mineral crystals are related to impaired mechanical function of cortical bone, Bone 34 (2004) 443–453, doi:10.1016/j.bone.2003.11.003.
[103] C.U. Brown, Y.N. Yeni, T.L. Norman, Fracture toughness is dependent on bone location—a study of the femoral neck, femoral shaft, and the tibial shaft, J. Biomed. Mater. Res. 49 (2000) 380–389, doi:10.1002/(SICI)1097-4636(20000305)49:3<380::AID-JBM11>3.0.CO;2-W.
[104] T.L. Norman, D. Vashishth, D.B. Burr, Fracture toughness of human bone under tension, J. Biomech. 28 (1995) 309–320, doi:10.1016/0021-9290(94)00069-G.
[105] L. Yan, A. Cinar, S. Ma, R. Abel, U. Hansen, T.J. Marrow, A method for fracture toughness measurement in trabecular bone using computed tomography, image correlation and finite element methods, J. Mech. Behav. Biomed. Mater. 109 (2020) 1–23, doi:10.1016/j.jmbbm.2020.103838.
[106] J. Shen, T.J. Marrow, D. Scotson, X. Jin, H. Wu, H. Chen, Combined evaluation of Young modulus and fracture toughness in small specimens of fine grained nuclear graphite using 3D image analysis, J. Nucl. Mater. 563 (2022) 153642, doi:10.1016/j.jnucmat.2022.153642.
[107] M. Peña Fernández, S.J. Sasso, S. McPhee, C. Black, J. Kanczler, G. Tozzi, U. Wolfram, Nonlinear micro finite element models based on digital volume correlation measurements predict early microdamage in newly formed bone, J. Mech. Behav. Biomed. Mater. 132 (2022) 105303, doi:10.1016/j.jmbbm.2022.105303.
[108] A. Braesch-Andersen, D. Wu, S.J. Ferguson, C. Persson, P. Isaksson, Application of phase-field fracture theories and digital volume correlation to synchrotron X-ray monitored fractures in human trabecular bone: a case study, J. Mech. Behav. Biomed. Mater. 135 (2022) 105446, doi:10.1016/j.jmbbm.2022.105446.
[109] A. Pacureanu, M. Langer, E. Boller, P. Tafforeau, F. Peyrin, Nanoscale imaging of the bone cell network with synchrotron X-ray tomography: optimization of acquisition setup, Med. Phys. 39 (2012) 2229–2238, doi:10.1118/1.3697525.
[110] C.A. Grant, L.J. Wilson, C. Langton, D. Epari, Comparison of mechanical and ultrasound elastic modulus of ovine tibial cortical bone, Med. Eng. Phys. 36 (2014) 869–874, doi:10.1016/j.medengphy.2014.03.012.
[111] J.H. Hubbell, S... Seltzer, Tables of X-Ray Mass Attenuation Coefficients and Mass Energy-Absorption Coefficients (version 1.4), Natl. Inst. Stand. Technol., Gaithersburg, MD, 2004.
[112] J.P. Suuronen, B. Hesse, M. Langer, M. Bohner, J. Villanova, Evaluation of imaging setups for quantitative phase contrast nanoCT of mineralized biomaterials, J. Synchrotron Radiat. 29 (2022) 843–852, doi:10.1107/S1600577522003137.
[113] A. Immel, A.Le Cabec, M. Bonazzi, A. Herbig, H. Temming, V.J. Schuenemann, K.I. Bos, F. Langbein, K. Harvati, A. Bridault, G. Pion, M.A. Julien, O. Krotova, N.J. Conard, S.C. Münzel, D.G. Drucker, B. Viola, J.J. Hublin, P. Tafforeau, J. Krause, Effect of X-ray irradiation on ancient DNA in sub-fossil bones - guidelines for safe X-ray imaging, Sci. Rep. 6 (2016) 1–14, doi:10.1038/srep32969.